Estimating Surface Current from a Satellite Image

by

Yun-chi Tseng

B.S. Tunghai University (Taiwan)
(1962)
M.Sc. Institute de Pesquisas Espacias (Brazil)
(1976)

SUBMITTED IN PARTIAL FULFILLMENT
OF THE REQUIREMENTS FOR THE
DEGREE OF

MASTER OF SCIENCE

at the

MASSACHUSETTS INSTITUTE OF TECHNOLOGY

May 1981

Signature of Author _____
Department of Meteorology &
Physical Oceanography

Certified by _____
Erik Mollo-Christensen
Thesis Supervisor

Accepted by _____
Peter H. Stone
Chairman, Departmental Graduate Committee

Estimating Surface Current from a Satellite Image

Table of Contents

ESTIMATING SURFACE CURRENT FROM A SATELLITE IMAGE

by

YUN-CHI TSENG

Submitted to the Department of Meteorology and Physical Oceanography
on 15 May 1981 in partial fulfillment of the
requirements for the degree of Master of Science

ABSTRACT

Surface current velocities can be estimated by careful use of surface characteristics obtained from a satellite image, together with other oceanographic data and simple oceanic dynamic approximations. Three simple approaches are used to estimate the propagation speed of a meandering current, the tangential velocity of a circulating eddy and the cross-current velocity of a deflected plume jet. Three case studies are also presented to verify these approaches. The results show that the estimated Gulf Stream propagation speed off Cape Hatteras is approximately 160 cm/sec; the maximum tangential velocity of the Gulf Stream warm core ring is approximately 180 cm/sec, and the cross-current velocity off Brazos Santiago Entrance Channel is of order 15 km/day. These estimated speeds are consistent with the representative oceanographic local data. This method offers a convenient and economical way to estimate the surface current from an image. However, careful approach selection and careful surface characteristic measurements from an image should be made in order to avoid serious errors.

Thesis Supervisor: Erik Mollo-Christensen, Professor of Oceanography

Acknowledgement

I wish to express my thanks to Professor Erik Mollo-Christensen for his suggestion of the topic, and his patience and guidance, not only in the period of the thesis writing, but also during my entire stay at M.I.T. I also thank him for his permission to use the MCIDAS system.

Thanks are also extended to Professor Keith D. Stolzenbach for his help in understanding his plume jet model, and to Peter Cornillon and Bob Thayer for their help in using the MCIDAS system for the image interpretation. Special thanks are also due to Affonso da S. Mascarenhas for various discussions.

I would like to thank Virginia Mills for her correction of the Chinese English and for her excellent job of typing.

Special thanks are given to my wife Kun Fan for her encouragement, patience and understanding, and to my sons Ko Li and Ra Nien for their understanding and patience.

I was supported by a fellowship from the Conselho Nacional de Desenvolvimento Cientifico e Technologico (CNPq) and by the Instituto de Pesquisas Espacias (INPE) of Brazil during my stay at M.I.T.

1. INTRODUCTION

1.1 Reviews of Surface Current Estimation from the Satellite Images

There are generally two broad methods to estimate ocean surface current quantitatively from a satellite image. The first method is to use the variation of sea surface characteristics obtained from successive images and their time differences as data to estimate surface current. The surface characteristics can be current boundaries, water masses, sea surface temperatures, ocean waves, a defleted plume, and many other sea surface and subsurface physical characteristics that can be sensed from satellites. The variation of these characteristics, usually measured in distance, with the time elasped of the corresponding images, can be used to estimate the surface current speeds. The second method is to attempt to apply some surface physical or subsurface characteristics which are obtained from one image, to simple mathematical approaches or models so that the surface current can be estimated accordingly. The surface characteristics can be the wave length of a surface wave or a meander, the diameter of an ocean ring or eddy, the defleted angle, the width and the curvature of a plume trajectory, etc. Usually a cloud-free satellite image, either infrared or visible, can show these features quite clearly. Obviously, the ideas of current estimation from these two methods are quite different. The first method tries to estimate the surface current from a sequence of successive images, while the second one attempts to estimate it from only one image, with the assistance of simple models or concepts.

Many investigators have used satellite images to detect the main currents around the world oceans. In the Gulf Stream region,

Wilkerson (1967) used Nimbus II meteorological spacecraft, carrying a television camera and two infrared radiometers, MRIR (Multi-channel Medium Resolution Infrared Radiometer) and HRIR (High Resolution Infrared Radiometer) to detect the boundary of Gulf Stream. The results showed that the position of the boundary are in good agreement between the satellite data and the ship and airplane observation. He also concluded that the combined data would be adequate for the study of synoptic changes of the Gulf Stream. Rao et. al. (1971), DeRycke and Rao (1973) and Stumpf and Rao (1975) discussed meanders and eddies of the Gulf Stream and their evolution, using satellite infrared data obtained from NOAA satellite series. Vukovich (1976) and Vukovich and Crissman (1978) studied a cold eddy on the eastern side of the Gulf Stream using NOAA satellite data and the ship data. The cold eddy was observed for about two weeks and moved southwest and finally entrained warm Gulf Stream water into its outer fringes. Maul and Hansen (1972) also investigated the western edge of the Gulf Stream surface front structure by ship, aircraft and satellite. They found that the sea surface temperatures at the Gulf Stream front obtained from HRIR of Nimbus II and IR scanner of aircraft are in quantitative agreement with the ship data. In other parts of the world ocean, for example, Duing and Szekieda (1971) observed the Somali Current for several years using Nimbus series satellites. They were able to determine the synoptic temperature of this region, which allowed them to study the development of the baroclinic structure of the Somali Current in response to the South-west Monsoon; Szekielda (1972) also observed the Bengula and Agulhas Currents, using Nimbus II HRIR; Warnecke et. al (1968, 1969, 1971)

repeatedly observed the Falkland and the Brazil currents and their thermal boundary using Nimbus series satellites and found that the boundary between these two currents is changing significantly every day. Recently a satellite radar altimetry technique has been developed, and provides a direct measurement of the sea surface topographic height. From such measurements the geostrophic component of the surface current can be computed directly (McGoogan, 1975). Leitão and Huang (1979) used the altimeter data of the Geos 3 satellite to detect the Gulf Stream surface boundaries. Results point out that the radar altimeter can sense the Gulf Stream boundaries with as much precision as the infrared-derived data analysis, and it also gives excellent agreement with the in situ data.

Almost all the investigators mentioned above observed the currents and current boundaries from satellite data and obtained sea surface temperature distributions and the positions of the boundaries. There were very few cases in which the current systems were related dynamically to their propagation of features and current speeds. Only very recently some investigators introduced the concept of dynamical interpretation of satellite data to estimate the surface current (speed). Tseng, et. al (1977) analyzed the thermal boundaries between the Falkland and the Brazil currents obtained from about seventy Nimbus IV and V THIR (Temperature humidity infrared radiometer). From this analysis, the speeds of the movement of the current fronts (east and west direction) in every season can be estimated. The results are in good agreement with ground truth data. Emery and Mysak (1980) applied two series of VHRR (Very High Resolution Radiometer) from NOAA 5, to

estimate the frontal wave propagation speeds off Vancouver Island and also to test a simple stability theory (Mysak, 1977). The winter series of three images exhibits cold tongues, extending seaward from Vancouver Island, which have separations (wavelengths), northwest phase speeds and growth rates consistent with a model of baroclinically unstable waves; an earlier summer series of eight images displays no such propagation behavior. Vukovich and Crissman (1980) also investigated the Gulf Stream western boundary eddies using NOAA-5 VHRR and ship data. The propagation speed of the wavelike western boundary was determined by analyzing successive positions of the wave crest versus time. Best estimates were obtained when crest positions were established from satellite imagery obtained at least two days apart. Although the spatial resolutions of the satellites are still low and the distortion of the images high, these investigators were attempting to estimate the current speed from many successive images. This method, as I classified it into the first method of estimating surface current, is a direct measuring method from images, not related to interpretations or models.

The second method of current estimation from a single image was proposed recently, because in general, many cloud-free successive images are difficult to obtain. Such methods attempt to estimate the current by employing some surface or subsurface characteristics of the ocean, which can be measured from any satellite image, to a simple mathematical model of ocean dynamics. In this approach, the surface current speed or average speed can be estimated accordingly. Very few papers have been published up to now, except for a paper written by Mollo-Christensen, et. al. (1981). Although they did not mention this idea

as clearly as I defined here, their intention to estimate the current velocity from an image is clear. Assuming barotropic instability waves to be excited by M_2 tidal oscillations, the phase speed is the wavelength divided by M_2 tidal period. This method applied to the Gulf Stream beyond Cape Hatteras give estimates of current speed in general agreement with in situ observations.

1.2 Objectives of Study

The second method defined in the previous section seems to promise to be a convenient and economical way to estimate surface current speed that can not be "seen" directly from an image, from the surface or subsurface characteristics, that can be obtained from an image. It is generally possible to assess the order of magnitude of velocity of a fluid from observations of some of the symptoms appearing on it. For example, the characteristics of meanders between two different speeding water masses can be related to their relative velocity; the diameter of a circulating ocean core ring can be related to its tangential velocity; a deflected plume trajectory or sea floor sedimentary distribution can be related to the longshore current; a surface wave pattern in a coastal area can be related to propagation by current; a surface or internal wave pattern in the open ocean can be related to the wave propagation in the ocean, etc. However, how to relate the surface or subsurface characteristics obtained from a satellite image to surface current speed is still a task left to research and exploration.

My purpose in this study is therefore intended to further explore this new idea and present methods of current investigations of the pos-

sible relations between the surface characteristics to the surface current, either through simple ocean models or through simple oceanography concepts. Some case studies will be chosen as examples to apply these methods. Due to the unavailability of the ground-truth data, the results will be compared only with some average data of those regions. Another purpose is intended to use the newly-installed RSMAS system for image interpretation. This system, equipped with a navigation subroutine enables us to measure the distance very rapidly and accurately.

2. SOME APPROACHES FOR SURFACE CURRENT ESTIMATION

2.1 Meander of the Current

The meanders of a current, which are good indicators of a current moving, can usually be observed from an IR image as well as a visible one. As we know, most of the principal currents in the world form sharp boundaries with their adjacent waters, and these meanders generally show up on the boundaries. The mechanism of forming meanders is still unclear; however, it is felt to be something related to the instabilities of the currents (Stommel, 1965). The most famous current, the Gulf Stream, has its meanders; the other currents, for example, the California Current, the Norweigian Current, the Kuroshio Current, the Brazil Current and the Falkland Current are also known for their meanders. These meanders can generally be observed clearly from the cloud-free satellite images, either infrared or visible.

Current meanders can be produced by the instability of the velocity profile across the current. Stommel (1965) noted that the meandering of the Gulf Stream may be due to instability, either barotropic, baroclinic, or both. In the theoretical studies of the meandering of the western boundary currents by Orlanski (1969) and Orlanski and Cox (1973), they concluded that the meandering of the Gulf Stream between Miami and Cape Hatteras can be attributed to baroclinic instability, and this result can also be compared with the observations. The baroclinic instability of the boundary currents may be a source mechanism for eddies in the eastern parts of mid-latitude basins and that these eddies may induce the sort of wave-like temperature pattern in the front dividing the cold slope water and the warm Gulf Stream.

Niiler and Mysak (1971) analyzed a barotropic constant f-model in which the velocity distribution and bottom topography of the continental shelf were approximated by segments of constant potential vorticity and depth. Unstable barotropic waves were possible in the model, because the potential vorticity was chosen to contain maxima in its distribution across the current. The arguments for these extrema are that the cyclonic shear in the inshore region raises the relative vorticity sufficiently to overcome the opposing effect of increasing depth of the shelf and slope. If the slope is small enough, a maximum occurs in potential vorticity. A region of anticyclonic shear on the seaward side of the Florida Current over a slowly varying depth yields a minimum in the cross-stream potential vorticity distribution. In studying a sequence of infrared images of the meanders off Cape Roman and Cape Fear, Stumpf and Rao (1975) suggested these meanders are influenced by topography and by instability of the Florida Current. In short, several mechanisms for generation in the Florida Current have been identified: barotropic and baroclinic instability in the presence of topography, bottom features forcing deflections and downstream lee waves, excitation of propagating waves by atmospheric forcing. Nonlinear mechanisms are yet to be explored, as are the effects of the downstream (Fofonoff, 1980).

In a model study of the stability of California Undercurrent off Vancouver Island, Mysak (1977) attempted to show that the mesoscale variations observed in the temperature and the currents off Vancouver Island may be due to baroclinic instability of the California Undercurrent which flows northward along the continental slope. He found

that the wavelengths of the most unstable waves agree very favorably with those associated with the cellular pattern in the sea surface temperature. A sequence of three VHRR infrared images from winter of 1979 exhibits a wavelength, phase speed and growth rate reasonably consistent with the baroclinically unstable model. It is possible that the observed wave is a marginally unstable, gravest mode nonlinear wave that has equilibrated (Emery and Mysak, 1980).

Hydrographic and current observations of the Norwegian Current show a considerable amount of low-frequency variability. Mysak and Schott (1977) considered a number of simple barotropic and baroclinic instability models of the mean flow in an attempt to explain these fluctuations. The theoretical results suggest that the current fluctuations most likely are due to baroclinic instability of the mean flow.

The Kuroshio Current, which flows along the coast of Japan, is also known to meander. The most conspicuous properties of the meanders are large and long-lived. Some meander continued as long as 10 years (Shoji, 1972). The Kuroshio meander south of Japan exists for a period of years, disappears for other years, and then reappears for another period. Decay of the meander appears to be a much slower process than generation. The three periods in which cold water masses occurred continuously are during 1935-44, 1953-55, and 1959-63. Observations indicate that it is present when the baroclinic transport of the Kuroshio is weak and is absent when the transport is large. When present, the wavelength of the meander is directly related to the magnitude of the transport. White and McCreary (1976) proposed that this large quasi-steady meander can be modeled as a Rossby lee wave phenomena

induced by a zonal baroclinic inertial jet passing past a coastal perturbation, scaled to represent Kyushu Island. However Solomon (1978) and Taft (1978) opposed this theory. Solomon objected primarily to the hypothesized influence of the Izu Ridge on the current path. Taft pointed out an apparent contradiction between theory and observation: in 1971 there was no meander in spite of the fact that relatively low values of transport were measured off Enshunada. McCreary and White (1979) discussed again their theory and explained their points of view. Although the theory of the Kuroshio meander is still being argued, the mechanisms for generation of meanders could be similar to the Gulf Stream, i.e., the barotropic and baroclinic instability in the presence of topography; bottom features forcing deflections and downstream lee waves; and excitation of propagating waves by atmospheric forcing.

The mechanisms of meander generation for the Brazil and the Falkland Currents are still unknown; however, the complexity of the meanders are observable from most of the cloud-free images (eg. Tseng, et. al., 1977; Szekielda, 1976).

2.1.1 Stable Meanders

Certain types of meandering might exist in which stratification and inertia are dynamically important. The density stratification of the real ocean is approximated by a two-layer system. If a meander is wide and stable, we can treat the problem as having uniform absolute vorticity. The absolute vorticity is conserved in the upper layer and, based on this, I present the following method to estimate the phase speed which is found to be very close to its current speed.

Vorticity conservation gives:

$$f + \frac{\partial v}{\partial x} = f(h/h_o) \tag{2.1}$$

where h is the depth of the upper layer; h_o the value of $h(x)$ at $x \longrightarrow \infty$; f the Coriolis parameter; v the tangential or meander velocity, which is close to the current velocity.

Where currents are curved or meandering, the centrifugal force accompanying the flow curvature must be taken into account. When the motion is anticyclonic, the centrifugal force augments the horizontal pressure gradient force, and when the motion is cyclonic it augments the Coriolis force f in both hemispheres. Then the equation of motion in the upper layer is

$$fv \pm v^2/r = g' \frac{\partial h}{\partial x} \tag{2.2}$$

where g' is reduced gravity; r the radius of curvature, which is assumed much greater than the width of the current (positive for cyclonic motion and negative for anti-cyclonic motion).

From Eq. (2.2) we can obtain v :

$$v = \frac{rf}{2} \pm \frac{1}{2}\sqrt{(rf^2 - 4g'\frac{\partial h}{\partial x})r} \qquad \text{(2.3a) for anticyclonic motion}$$

or

$$v = -\frac{rf}{2} \pm \frac{1}{2}\sqrt{(rf^2 + 4g'\frac{\partial h}{\partial x})r} \qquad \text{(2.3b) for cyclonic motion}$$

In Eq. (2.3a) we have to choose the minus sign, and in Eq. (2.3b) we choose the positive sign, in order to make v zero when the pressure gradient vanishes. Eq. (2.3a) shows that, when $4g'\frac{\partial h}{\partial x} > rf^2$, v becomes imaginary. Therefore, the pressure gradient is less than the Coriolis force in the anticyclonic case. We now consider the cyclonic case, and substitute h from Eq. (2.1) into (2.2). We obtain

$$v + \frac{v^2}{Rrc} = \frac{1}{R^2}\frac{\partial^2 v}{\partial x^2} \qquad (2.4)$$

where $R = \frac{f}{\sqrt{gh_0}}$; $C = \sqrt{gh_0}$

We regard the nonlinear term as small in comparison with others, and express v in series form and proceed as Stommel (1965):

$$v = v_0 + \frac{v_1}{rR} + \frac{v_2}{(rR)^2} + \cdots \qquad (2.5)$$

and $v_0 >> v_1 >> v_2 \cdots$

Substitute this series in Eq. (2.4) and obtain

$$\begin{aligned} v_0 &= R^{-2}\,\partial^2 v_0 \\ v_1 + C^{-1} v_0^2 &= R^{-2}\,\frac{\partial^2 v_1}{\partial x^2} \\ v_2 + C^{-1} 2 v_0 v_1 &= R^{-2}\,\frac{\partial^2 v_2}{\partial x^2} \\ &\cdots\cdots \end{aligned} \qquad (2.6)$$

The solutions are

$$\begin{aligned} v_0 &= C e^{-Rx} \\ v_1 &= \frac{C}{3} e^{-2Rx} \\ v_2 &= \frac{C}{12} e^{-3Rx} \\ &\cdots\cdots \end{aligned} \qquad (2.7)$$

We can also find the first approximation of h from Eq. (2.2) by direct integration

$$h = -\frac{1}{g'}\int_x^\infty \left(f v + \frac{v^2}{r}\right) dx$$

$$= -\frac{1}{g'}\int_x^\infty \left[f\left(v_0 + \frac{v_1}{rR}\right) + \frac{v_0^2}{r}\right] dx$$

$$h = h_0\left(1 - e^{-Rx} - \frac{2}{3Rr}\, e^{-2Rx}\right) \tag{2.8}$$

where h_0 is the value of $h(x)$ as $x \longrightarrow \infty$. The value of x as h vanishing is approximated by

$$x \approx \frac{2}{3R^2 r} \tag{2.9}$$

The total transport of the current T is

$$T = \int_{x=\frac{2}{3R^2r}}^{\infty} v h\, dx \approx C\, h_0\left(\frac{1}{2R} - \frac{1}{6R^2 r}\right) \tag{2.10}$$

Suppose the shape of the meander is

$$x = x_o \cos (ly - \sigma t) \tag{2.11}$$

where x_o is the amplitude of the meander, l is wave number, σ is the frequency. At time $t=0$, the rate of increase of volume of water between $ly=0$ and $ly=\pi$ due to the motion of the meander is $2 x_o h_o (\sigma/l)$. This, of course, must be equal to the excess of transport through a crest ($ly=0$) over that through a trough ($ly=\pi$), $C h_o / 3R^2 r$. But at $t=0$ and $y=0$, the radius of curvature r is also given by $r^{-1} = \partial^2 x / \partial y^2 = x_o l^2$, hence the phase speed advances parallel to the y axis C_y is

$$C_y = \frac{\sigma}{l} = \frac{C^3 l^2}{6 f^2} \tag{2.12}$$

where wave number, l, can be calculated from wave length λ which usually can be measured from an image. $C = \sqrt{g' h_o}$ is usually known in the current. For example, in the Gulf Stream area, the typical value of $g' \simeq 1$ cm sec^{-2}, $h_o \simeq 1$ km, and yields $c = 3.2$ ms^{-1}. For a meander wave length of 300 km, the phase speed is therefore about 23 cm/sec. For a meander wave length 150 km, the phase speed becomes 95 cm/sec.

2.1.2 Baroclinic Instability

When a boundary current is considered to be baroclinically unstable, it is due to the vertical shear in the basic current. This also implies a horizontal temperature gradient and therefore the presence of available potential energy. Otherwise the process only depends on the existence of horizontal shear in the basic current. This kind is a barotropic instability. Although all currents in the atmosphere and the ocean possess, to varying degrees, both horizontal and vertical shear, it is helpful to simplify the situation if we consider one of them as dominant in a current system. In order to discuss baroclinic instability, and hopefully to relate it to our purpose, i.e., to estimate the surface current, at least to estimate a range of the current speed or the current speed as marginally unstable. I would like to consider the simplest two-layer model. The two layers of fluid, each with different constant density, lie on a plane rotating with angular velocity $f_0 + \beta y$. The lighter fluid lies above the heavier one. The fluid is bounded above by a rigid horizontal plane. The lower boundary is nearly flat and the mean distances of the two layers are h_1 and h_2 respectively. The deviation of the lower boundary from perfect flatness is given by the equation for the bottom $z_* = d_* \eta_B(x)$, where d_* is an amplitude measure of the bottom variation and $\eta_B(x)$ yields the shape of the bottom, as shown in Fig. 2.1 on the following page.

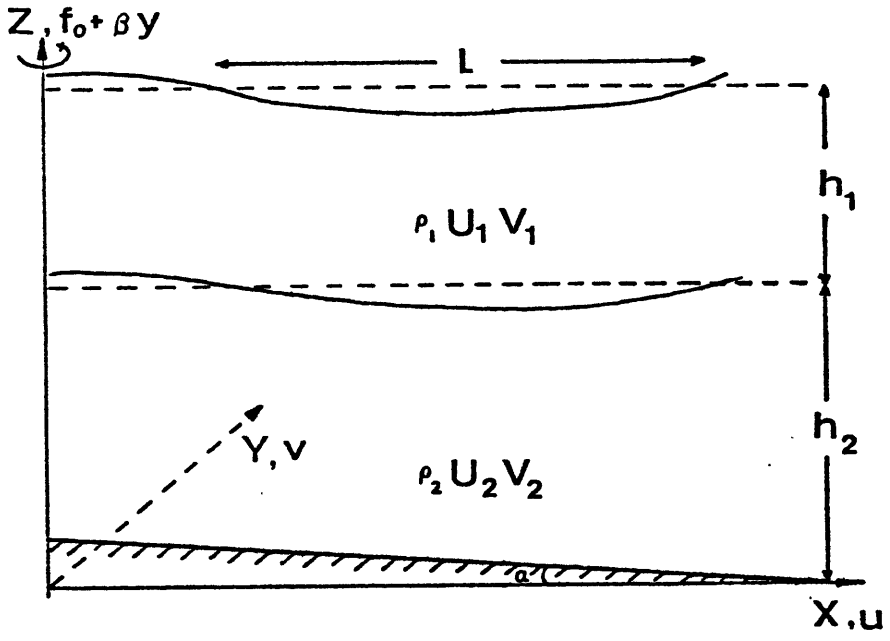

Fig. 2.1 Geometry of Two-layer Model

For small Rossby number $R_o = U/f_o L$, the governing non-dimensional equations of motion are the quasi-geostrophic potential vorticity equations (Pedlosky, 1976).

$$\left(\frac{\partial}{\partial t} + \frac{\partial \psi_1}{\partial x}\frac{\partial}{\partial y} - \frac{\partial \psi_1}{\partial y}\frac{\partial}{\partial x}\right)\left[\nabla^2\psi_1 - F_1(\psi_1 - \psi_2) + \beta y\right] = T_1(x,y,t) \qquad (2.13)$$

$$\left(\frac{\partial}{\partial t} + \frac{\partial \psi_2}{\partial x}\frac{\partial}{\partial y} - \frac{\partial \psi_2}{\partial y}\frac{\partial}{\partial x}\right)\left[\nabla^2\psi_2 - F_2(\psi_2 - \psi_1) + \beta y + \delta B(x)\right] = T_2(x,y,t) \qquad (2.14)$$

and associated boundary conditions

$$\frac{\partial \psi_n}{\partial y} = 0 \quad , \text{at } x = 0, 1 \quad , \; n = 1, 2$$

where x and y are longitude and latitude coordinates, ψ_1 and ψ_2 are the non-dimensional geostrophic streamfunctions.

$$F_1 = \frac{f_0^2 L^2}{g(\Delta\rho/\rho) h_1}$$

$$F_2 = \frac{f_0^2 L^2}{g(\Delta\rho/\rho) h_2}$$

$$\Delta\rho/\rho = (\rho_2 - \rho_1)/\rho_0$$

$$\delta B(x) = \frac{f_0 L}{U} \frac{d_*}{h_2} \eta_B(x)$$

$$\delta = d_*/h_2 \leq O(1)$$

$$\nabla^2 = \frac{\partial^2}{\partial x^2} + \frac{\partial^2}{\partial y^2}$$

$$\beta = \beta_0 \frac{L^2}{U}$$

$$h_2 = h - h_1$$

The function $T_k(x, y, t)$ are some unspecified sources of potential vorticity for each layer which will be responsible for altering the mean potential vorticity of the current along its path. We want to generalize the conditions and assume there are nonzonal basic flows in either x or y direction. Nonzonal basic flows imply the existence of an external forcing field. This forcing field can be wind stress on

the surface or friction force at the interface between layers, or bottom friction force. Consider now the basic state to examine the stability of the flow. We write

$$\psi_1 = \vec{\psi}_1 = U_1 y + V_1 x + \phi_1(x, y, t) \tag{2.15}$$

$$\psi_2 = \vec{\psi}_1 = U_2 y + V_2 x + \phi_2(x, y, t) \tag{2.16}$$

where U_1, U_2, V_1, V_2 are constant. If Eqs. (2.15) and (2.16) are inserted into Eqs. (2.13) and (2.14), linearized and neglected the second order of ϕ_n; we obtain the perturbation equations

$$\left(\frac{\partial}{\partial t} - U_1 \frac{\partial}{\partial x} + V_1 \frac{\partial}{\partial y}\right)\left[\nabla^2 \phi_1 - F_1(\phi_1 - \phi_2)\right] - F_1 \frac{\partial \phi_1}{\partial x}(U_1 - U_2) + \beta \frac{\partial \phi_1}{\partial x} + F_1 \frac{\partial \phi_1}{\partial y}(V_1 - V_2) = 0 \tag{2.17}$$

$$\left(\frac{\partial}{\partial t} - U_2 \frac{\partial}{\partial x} + V_2 \frac{\partial}{\partial y}\right)\left[\nabla^2 \phi_2 + F_2(\phi_1 - \phi_2)\right] + F_1 \frac{\partial \phi_2}{\partial x}(U_1 - U_2) + \beta \frac{\partial \phi_2}{\partial x} - F_2 \frac{\partial \phi_2}{\partial y}(V_1 - V_2) + T \frac{\partial \phi_2}{\partial y} = 0 \tag{2.18}$$

where $T = \alpha f L^2/h_2 U$ (topographic parameter). For $\alpha < 0$ the bottom slopes upward toward the coast as shown in Fig. 2.1 .

The associated boundary conditions are

$$\frac{\partial \phi_n}{\partial y} = 0 \qquad \text{at} \qquad x = 0, 1 \; ; \; n = 1, 2$$

If we seek traveling wave solutions of Eqs. (2.17) and (2.18)

$$\phi_1 = Re \left\{ A_m e^{i(ly - \sigma t)} \sin m\pi x \right\}$$

$$\phi_2 = Re \left\{ B_m e^{i(ly - \sigma t)} \sin m\pi x \right\}$$

without loss of generality we take $l > 0$ and $A_m, B_m > 0$

Also we can choose $A_m = \mu B_m$, where $\mu = \mu_r + i\mu_i$

Substituting ϕ_1 and ϕ_2 into Eq. (2.17) and (2.18), we obtain

$$A_1 \left[K^2 (\sigma + U_1 k - V_1 l) + F_1 (\sigma + U_2 k - V_2 l) + \beta k \right]$$

$$- B_1 F_1 (\sigma + U_1 k - V_1 l) = 0 \qquad (2.19)$$

$$A_1 F_2 (\sigma + U_2 k - V_2 l) - B_1 [K^2 (\sigma + U_2 k - V_2 l) + F_2 (\sigma + U_1 k - V l) + \beta k + T l] = 0 \qquad (2.20)$$

Solve Eqs. (2.19) and (2.20), and obtain the dispersion relation

$$a \sigma^2 + b \sigma + d = 0 \qquad (2.21)$$

and $$\sigma = -\frac{b}{2a} \pm \frac{1}{2a} (b^2 - 4ad)$$

where $$a = K^2 (K^2 + F_1 + F_2)$$

$$b = K^4 (\hat{U}_1 + \hat{U}_2) + 2 K^2 (F_1 \hat{U}_2 + F_2 \hat{U}_1 + \hat{\beta}) + (F_1 + F_2) \hat{\beta} + (K^2 + F_1) \hat{T}$$

$$d = K^4 \hat{U}_1 \hat{U}_2 + K^2 [\hat{U}_1 (F_2 \hat{U}_1 + \hat{\beta} + \hat{T}) + \hat{U}_2 (F_1 \hat{U}_2 + \hat{\beta})] + [(F_1 \hat{U}_2 + \hat{\beta})(F_2 \hat{U}_1 + \hat{\beta} + \hat{T}) - F_1 F_2 \hat{U}_1 \hat{U}_2]$$

and

$$K^2 = l^2 + k^2 \quad , \quad \hat{\beta} = \beta k$$
$$\hat{U}_1 = U_1 k - V_1 l \quad , \quad \hat{T} = T l$$
$$\hat{U}_2 = U_2 k - V_2 l \quad , \quad k = m\pi$$

If we change frequency σ' to phase speed c . Eq. (2.21) becomes

$$a' c^2 + b' c + d' = 0$$

$$c = -\frac{b'}{2a'} \pm \frac{1}{2a'} (b'^2 - 4a'd')^{\frac{1}{2}} \tag{2.22}$$

where

$$a' = K^2 (K^2 + F_1 + F_2)$$

$$b' = K^4 (\tilde{U}_1 + \tilde{U}_2) + 2K^2 (F_1 \tilde{U}_2 + F_2 \tilde{U}_1 + \tilde{\beta}) + (F_1 + F_2) \tilde{\beta} + (K^2 + F_1) \tilde{T}$$

$$d' = K^4 \tilde{U}_1 \tilde{U}_2 + K^2 [\tilde{U}_1 (F_2 \tilde{U}_1 + \tilde{\beta} + \tilde{T}) + \tilde{U}_2 (F_1 \tilde{U}_2 + \tilde{\beta})] + [(F_1 \tilde{U}_2 + \tilde{\beta})(F_2 \tilde{U}_1 + \tilde{\beta} + \tilde{T}) - F_1 F_2 \tilde{U}_1 \tilde{U}_2]$$

and $$\tilde{U}_1 = \hat{U}_1 / K \ , \ \tilde{U}_2 = \hat{U}_2 / K \ , \ \tilde{\beta} = \hat{\beta} / K \ , \ \tilde{T} = \hat{T} / K$$

The phase speed c may be written in terms of its real and imaginary parts, and $c = c_r + ic_i$ where $c_r = \mathrm{Re}(\sigma')/K$, $c_i = \mathrm{Im}(\sigma')/K$.

A nontrivial solution exists for arbitrary Am provided that

$$\mu_r = \frac{K^2}{F_1} + \frac{(c_r+\tilde{U}_2)(c_r+\tilde{U}_2)+c_i^2}{(c_r+\tilde{U}_1)^2+c_i^2} + \frac{\tilde{\beta}(c_r+\tilde{U}_1)}{F_1[(c_r+\tilde{U}_1)^2+c_i^2]} \tag{2.23a}$$

$$\mu_i = \frac{c_i(\tilde{U}_1-\tilde{U}_2)}{(c_r+\tilde{U}_1)^2+c_i^2} - \frac{\tilde{\beta}c_i}{F_1[(c_r+\tilde{U}_1)^2+c_i^2]} \tag{2.23b}$$

The velocity components in each layer are computed from the relation

$u_n = -\phi_{ny}$ and $v_n = \phi_{nx}$. Their forms take

$$\begin{aligned}
u_1 &= l A_m e^{\sigma_i t} \sin(ly - \sigma_r t) \sin m\pi x \\
v_1 &= m\pi A_m e^{\sigma_i t} \cos(ly - \sigma_r t) \cos m\pi x \\
u_2 &= l B_m e^{\sigma_i t} \sin(ly - \sigma_r t + \alpha) \sin m\pi x \\
u_2 &= m\pi B_m e^{\sigma_i t} \cos(ly - \sigma_r t + \alpha) \cos m\pi x
\end{aligned} \tag{2.24}$$

where $\sigma_r = Re(\sigma)$, $\sigma_i = Im(\sigma)$

$B_m = |\mu| A_m$, $\tan\alpha = \mu_i / \mu_r$

The solution of phase speed in Eq. (2.21) can generally determine the instability criteria of the flow motion. In order to simplify the problem, we assume the following cases.

Case I: $U_2 = V_2 = 0$ and $T = 0$. This means no mean flows in either direction in lower layer and without topography. Substitute $U_1 = -U_1$ in Eqs. (2.19) and (2.20). We obtain

$$A_1[(K^2+F_1)(c-\tilde{U}_1)+\tilde{\beta}+F_1\tilde{U}_1]-B_1F_1(c-\tilde{U}_1)=0$$
$$A_1(c)F_2-B_1[c(K^2+F_2)+\tilde{\beta}-F_2\tilde{U}_1]=0 \qquad (2.25)$$

These equations are exactly equal to the non-zonal two-layer equations (Pedlosky, 1979), and

$$c=-\frac{1}{2b'}\pm\frac{1}{2b'}(b'^2-4a'd')^{\frac{1}{2}}$$

where

$$a'=K^2(K^2+F_1+F_2)$$

$$b'=-\tilde{U}_1K^2(K^2+2F_2)+\tilde{\beta}(2K^2+F_1+F_2)$$

$$d'=(-K^2\tilde{U}_1+\tilde{\beta})(-F_2+\tilde{\beta})$$

In particular, the minimum critical shear required for instability is either

$$\tilde{U}_{c+} = \frac{\tilde{\beta}}{F_2} \quad , \quad \tilde{U}_1 > 0 \tag{2.26a}$$

$$\tilde{U}_{c-} = -\frac{\tilde{\beta}}{F_1} \quad , \quad \tilde{U}_1 < 0 \tag{2.26b}$$

However, for $k = 0$, $\tilde{\beta}$ will vanish, so that any shear will be unstable to such a disturbance as long as $\tilde{U}_1 \neq 0$ for $k = 0$. This requires only that the shear flow have some nonzero component in the y-direction. That is for $k = 0$

$$c_i = \frac{V_1}{2} \frac{\left[4 F_1 F_2 - l^4\right]^{\frac{1}{2}}}{l^2 + F_1 + F_2}$$

Thus, as long as $l^2 < 2 (F_1 F_2)^{\frac{1}{2}}$, the basic flow will be unstable to the mode with $k = 0$, and therefore no minimum shear is required for instability.

Case II: $U_1 = U_2 = 0$. This means no zonal mean flows. Eqs. (2.19) and (2.20) become

$$a = K^2 (K^2 + F_1 + F_2)$$

$$b = -l \left[a (V_1 + V_2) + K^2 (V_1 - V_2)(F_2 - F_1) + (F_1 + F_2) \frac{k \beta}{l} - (K^2 + F_1) T + 2K^2 \frac{\beta k}{l} \right]$$

$$d = l^2 \left\{ a V_1 V_2 + K^2 (V_1 - V_2)(V_1 F_2 - V_2 F_1) - T\left(K^2 V_1 + F_1 V_1 - \frac{\beta k}{l^2} \right) \right.$$

$$\left. - \frac{\beta k}{l} \left[K^2 (V_1 + V_2) + F_1 V_2 + F_2 V_1 - \frac{\beta k}{l} \right] \right\}$$

Case III: When rotation of earth can be neglected, i.e. $\beta = 0$, also no zonal flows, i.e., $U_1 = U_2 = 0$. Then

$$a = K^2 (K^2 + F_1 + F_2)$$

$$b = -l \left[a (V_1 + V_2) + K^2 (V_1 - V_2)(F_2 - F_1) - T (K^2 + F_1) \right]$$

$$d = l^2 \left[a V_1 V_2 + K^2 (V_1 - V_2)(V_1 F_2 - V_2 F_1) - T (K^2 V_1 + F_1 V_2) \right]$$

These equations are for a baroclinic two-layer model with meridional flow in both layers (Mysak, 1977, Mysak and Schott, 1977).

Case IV: When either no mean flow in x direction or in y direction, i.e., $U_1 = U_2 = V_1 = V_2 = 0$, and also $\beta = 0$, then

$$\sigma = l (K^2 + F_1) T \Big/ K^2 (K^2 + F_1 + F_2) \qquad (2.27)$$

which represents the dispersion relation for a topographic planetary wave in a two-layer system which propagates in the y direction. In principle, the dispersion relations stated above allow us to find a criteria shear or shears to be unstable, which is a function of wave number. Referring to some other parameters of a current system, a wave length obtained from a satellite image can be obtained from a satellite image to be unstable. Its corresponding wave speeds can also be varified to be unstable.

2.2 Eddies or Core Rings in the Ocean

A warm or cold core ring in the ocean is a flow structure associated with an isolated mass of anomalous water, significantly warmer or colder, saltier or fresher, that its surroundings. The rings are approximately circular structures which are generally considered by the pinching off of a current meander. Many currents are known by their "rings". The Gulf Stream and the Kuroshio are the most well-known. The East Australian Current (Andrews and Scully-Power, 1976), the central North Pacific (Bernstern and White, 1974), in the Arctic Ocean (Newton, et. al., 1974; Hunkins, 1974), etc. have also been found to have a large or small ocean eddy.

Many investigators have already studied or observed cold or warm core rings in the Gulf Stream. As far as we know, the cold core rings of the Gulf Stream, formed south of the stream, have a central core of very cold slope water surrounded by a ring of high-velocity cyclonic currents. The warm core rings, formed to the north of the Stream, are an isolated lens of warm Sargasso water lying on top of the colder slope water

surrounded by a ring of high-velocity anticyclonic current. While the exact physics of the separation process is not known, it is known that the meanders of the stream become sufficiently large to form detached cold eddies (Parker, 1971; Fuglister, 1972; Gotthardt, 1973) and warm eddies to the north (Saunders, 1971) of the stream at irregular intervals. A cold ring may keep its integrity for as long as two years (Richardson, et. al., 1973) with warm water slowly encroaching, or it may be reentrained in the Gulf Stream.

In the region of the Kuroshio Current east of Japan, large-scale anticyclonic eddies are generated on its left side and cyclonic eddies on its right. The anticyclonic eddies have warm cores which are considered to represent water separated from the protruding ridges of the meandering main stream axis. Many research vessels operated by several institutions of the Japanese Government have cooperatively taken oceanographic observations in a grid over the sea area adjacent to the Japanese Islands almost simultaneously for 17 years, from 1957 through 1973. They provided the characteristics of 154 examples of typical warm eddies at the confluence zone of the Kuroshio and the Oyashio Currents. The eddies are elliptical forms with an average diameter of about 130 km (70 n mi), and usually move to the north or northeast with a speed of 0.5 - 3.6 km/day (0.3 - 2.0 n mi/day) along the contours of the continental slope. Their sizes and maximum core temperatures decrease as they move to the north (kitano, 1975). The depth of the warm eddy in the Kuroshio and the Kuroshio Extension is about 200 m, shallower than in the Gulf Stream (Kawai, 1972). The cold eddies were found south of the coast of Japan, associated with the large-scale

meandering of the Kuroshio. The cold eddies have low salinity and high oxygen content at depths between 200 m and 500 m (Masuzawa, 1955a, 1955b, 1956) in the Kuroshio Extension. The temperatures of cold eddies are below 3 or 4°C which seems to be lower than those in the Gulf Stream (LaFond, 1968).

Many investigators also found warm core eddies off east Australia. Wyrtki (1962) suggested that these eddies are separated from the main current and probably drift south down the coast, and the eddy diameters range from 200-250 km while drift rates are estimated 5-8 km/day (Boland and Hamon, 1970). Andrews and Scully-Power (1976) observed an intense, anticyclonic warm winter eddy off the east coast of Australia with an airborne radiation thermometer, expendable bathythermographs, and a continuously recording surface thermosalinograph. They found the eddy had a diameter of 250 km and a mixed layer depth extending to over 300 m in the core. A strong current ring was present halfway from the center to the edge of the eddy with the surface speeds ranging from 0.6 to 1.78 m sec^{-1}. The interior deep mixed layer was completely enclosed by a shell of isothermal water, and indicated that large-scale entrainment of surface water may be an important feature of eddy generation off East Australia.

In the Atlantic area, Phillips (1966) and Swallow (1971) found baroclinic eddies in the deep North Atlantic with length scales from 300 to 400 km and time periods of 50 to 100 days, and also in upper 500 m (Bernstein and White, 1974). Based on the results of closely spaced BT and fixed moorings data in this area, Bernstein and White (1974) indicate that the eddies are not composed of a uniform water mass

carried along by the mean flow, and propagate at a phase speed in excellent agreement with the non-dispersive baroclinic planetary waves ($\sim$ 4.2 cm/sec). In the mid-latitude North Pacific Ocean eddies with remarkable similarity in scales to the North Pacific Ocean were also found (Bornstein and White, 1977). Even these eddies are present further east with the California Current (Reid, et. al., 1963; Bernstein, et. al., 1976).

In the Arctic, on the other hand, smaller eddies of 5-20 km diameter have been observed (Newton, et. al., 1974; Hunkins, 1974) and some of them are believed to be originally related to baroclinic instability (Hunkins, 1974). Also, many small eddies and related low-frequency current motions have been observed in relatively small bodies of water such as gulfs, straits and lakes (Otterman, 1974; Simons, 1976; Chang, et. al., 1976).

Usually ocean eddies have been modeled in two different ways. One is a diffusive model with consideration of an isolated vertex on the f-plane (Molinari, 1970; Schmitz and Vastano, 1975), and the other is the studies of mesoscale eddies on a β-plane with numerical models (Bretherton and Karweit, 1975; Flierl, 1977). However, a simple two-layer frictionless model based on the assumption of geostrophic balance and inviscid constant potential was developed by Csanady (1979) and improved by Flierl (1979) in order to discuss cold-core more accurately. Later Nof (1981) applied this model to test his model for the shape and structure of an Amazonian lens, and the results seem to be qualitative agreement. This simple model is applicable to calculate the tangential velocity of an ocean ring and to predict the

decay lifetime of a core ring. Although the tangential speeds obtained from some examples in the Gulf Stream seem too large, this model is still a good example and method to relate the current speeds to the surface characteristics obtained from a satellite image.

The equations for conservation of momentum in the radial direction and the potential vorticity equation in cylindrical coordinates for f-plane are

$$\frac{\partial u_r}{\partial t} + u_r \frac{\partial u_r}{\partial r} + \frac{u_\theta}{r} \frac{\partial u_r}{\partial \theta} - \frac{u_\theta^2}{r} - f u_\theta = - g' \frac{\partial h}{\partial r} \tag{2.28}$$

$$\left(\frac{\partial}{\partial t} + u_r \frac{\partial}{\partial r} + \frac{u_\theta}{r} \frac{\partial}{\partial \theta}\right)\left[\left(\frac{\partial u_\theta}{\partial r} + \frac{u_\theta}{r} - \frac{1}{r} \frac{\partial u_r}{\partial \theta} + f \right) / h \right] = 0 \tag{2.29}$$

where h is the depth of the moving upper layer, g' is its reduced gravity, and U_r and U_θ are velocities along r and θ directions. The potential vorticity theorem then states that

$$\frac{\partial u_\theta}{\partial r} + \frac{u_\theta}{r} - \frac{1}{r} \frac{\partial u_r}{\partial \theta} + f = h\, F(\psi) \tag{2.30}$$

where ψ is the stream function, and considered the simplest case in which the potential vorticity is conserved, as indicated by Stommel (1965), i.e., $F(\psi) = f / h_o$ and h_o is effectively the initial thermocline depth for most of the Gulf Stream water. Further, assuming that the motion on the upper layer is purely tangen-

tial, i.e., $u_r = 0$ and $\frac{\partial}{\partial\theta} = 0$, then Eqs. (2.28) and (2.30) reduce to

$$\frac{u_\theta^2}{r} + f u_\theta = g' \frac{\partial h}{\partial r} \tag{2.31}$$

$$\frac{\partial u_\theta}{\partial r} + \frac{u_\theta}{r} + f = \frac{h}{h_0} f \tag{2.32}$$

In Eq. (2.31), there are several cases of approximation:

1) Geostrophic balance, i.e. $f u_\theta \simeq g' \frac{\partial h}{\partial r}$ and $\frac{u_\theta^2}{r}$ can be neglected;
2) Inertial balance, i.e., $\frac{u_\theta^2}{r} \simeq f u_\theta$ and $g' \frac{\partial h}{\partial r}$ can be neglected;
3) Cyclostrophic balance, i.e., $\frac{u_\theta^2}{r} \simeq g' \frac{\partial h}{\partial r}$ and $f u_\theta$ can be neglected.

Refering to the first approximation, Csanady (1979) assumed that the approximation of geostrophic balance, that it, U_θ^2 term in Eq. (2.31), can be neglected, hence

$$u_\theta = \frac{g'}{f} \frac{\partial h}{\partial r} \tag{2.33}$$

Substitute Eq. (2.33) in (2.32), obtain

$$\frac{d^2 h}{dr^2} + \frac{1}{r} \frac{dh}{dr} - \frac{h}{R^2} = - \frac{h_0}{R^2}$$

The solution with the boundary condition $h = 0$ at $r = r_o$

$$h = h_o \left[1 - \frac{I_o(r/R)}{I_o(r_o/R)} \right] \tag{2.34}$$

and the tangential velocity distribution of a ring is

$$u_\theta = \frac{g'}{f}\frac{dh}{dr} = -Rf \frac{I_1(\frac{r}{R})}{I_o(\frac{r_o}{R})} \tag{2.35}$$

where $R^2 = g' h_o / f^2$, I_n is the Bessel function of order n.

From a cloud-free satellite IR image (or visible) it is possible to measure the radius of an eddy or a core ring very accurately and quickly by means of the MCIDAS system at MIT. This measured radius shall be very close to the real r_o , i.e., the radius when h approaches zero. The values of h_o , which are effectively the initial thermocline depths for the current systems, are also known for most currents, and accordingly R is known. The tangential velocity distribution of such a ring can be calculated from Eq. (2.35).

It is possible to calculate the rate at which a ring is losing its available energy and then to estimate the approximate time scale for the initial rate of decay due to friction and due to entrainment.

$$V = \int_o^{r_o} 2\pi r h \, dr = \pi h_o r_o^2 \left[1 - \frac{2R}{r_o} \frac{I_1(r_o/R)}{I_o(r_o/R)} \right] \tag{2.36}$$

The decay time scale due to entrainment may be calculated from

$$t_e = \frac{V}{dV/dt} = \frac{\gamma_v}{\gamma_e} \frac{1}{2\lambda} \frac{f r_o}{g'} \tag{2.37}$$

and a time scale for the initial rate of decay due to friction is

$$t_f = \frac{E_k + E_p}{dE/dt} = \frac{\gamma_k + \gamma_p}{\gamma_s} \frac{3}{4C_d} \frac{f r_o}{g'} \tag{2.38}$$

where

$$E_p = \int \frac{g'h}{2} 2\pi r h dr = \gamma_p \frac{\pi g' h_o^2 r_o^2}{2}$$, the total potential energy

$$E_k = \int \frac{v^2}{2} 2\pi r h dr = \gamma_k \frac{\pi g' h_o^2 r_o^2}{2}$$, the total kinetic energy

$$\frac{dE}{dt} = \int_0^{r_o} C_d u_\theta^2 2\pi r dr = -\gamma_s \frac{2\pi C_d}{3} r_o f^3 R^4$$

$$\frac{dV}{dt} = \int_0^{r_o} \lambda v 2\pi r dr = r_e 2\pi\lambda \frac{g' h_o r_o}{f}$$

and the parameters

$$\gamma_p = \frac{2R^2}{r_o^2} \int_0^{r_o/R} \left[1 - \frac{I_o(r/R)}{I_o(r_o/R)} \right]^2 \frac{r}{R} \, d\left(\frac{r}{R}\right)$$

$$\gamma_k = \frac{2R^2}{r_o^2} \int_0^{r_o/R} \frac{I_1^2(r/R)}{I_o^2(r_o/R)} \left[1 - \frac{I_o(r/R)}{I_o(r_o/R)} \right] \frac{r}{R} \, d\left(\frac{r}{d}\right)$$

$$\gamma_s = \frac{3R}{r_o} \int_0^{r_o/R} \frac{I_1^3(r/R)}{I_o^3(r_o/R)} \frac{r}{R} \, d\left(\frac{r}{R}\right)$$

$$\gamma_e = \frac{R}{r_o} \int_0^{r_o/R} \frac{I_1(r/R)}{I_o(r_o/R)} \frac{r}{R} \, d\left(\frac{r}{R}\right)$$

$$\tau_i = C_d u_\theta^2 , \qquad \text{interface stress}$$

C_d is a drag coefficient $\simeq$ $0.3 \sim 0.5 \times 10^{-3}$ in the case where the interface is sharp and stable (Csanady, 1978).

w , entrainment velocity , $= \lambda u_\theta$

λ is a proportional constant.

Eqs. (2.27) and (2.28) are very similar to each other, except for the different constants C_d and λ . The order of magnitude of the two time scales t_f and t_e depends on that of the parameter C_d and λ . When the case for very diffuse pycnocline, t_f and t_e may have the same order of magnitude. When the density gradient at the core of pycnocline is large, turbulence is suppressed. In

this case ring decay due to entrainment can be neglected in comparing to frictional decay.

The geostrophic approximation is fairly accurate for the warm core rings, but not very good for the cold core rings (Flierl, 1979). In case the centrifugal terms are not neglected, we may eliminate one of the variables h by substituting h from Eq. (2.32) into Eq. (2.31). We obtain a differential equation with U_θ only.

$$\frac{\partial^2 u_\theta}{\partial r^2} + \frac{1}{r}\frac{\partial u_\theta}{\partial r} - u_\theta\left(\frac{1}{r^2} + \frac{1}{R^2}\right) - \frac{1}{fR^2}\frac{u_\theta^2}{r} = 0 \tag{2.39}$$

and

$$h = \frac{h_o}{f}\left(\frac{\partial u_\theta}{\partial r} + \frac{u_\theta}{r} + f\right) \tag{2.40}$$

Scaling Eq. (2.39) and (2.40) by $r \sim R$, $U_\theta \sim U$, $h \sim h_o$ and set $\varepsilon = U/fR$ (the Rossby number), we obtain the non-dimensional equations

$$\frac{\partial^2 u_\theta}{\partial r^2} + \frac{1}{r}\frac{\partial u_\theta}{\partial r} - u_\theta\left(\frac{1}{r^2} + 1\right) - \varepsilon\frac{u_\theta^2}{r} = 0 \tag{2.41}$$

$$h = 1 + \varepsilon\left(\frac{\partial u_\theta}{\partial r} + \frac{u_\theta}{r}\right) \tag{2.42}$$

For warm core rings, the boundary conditions are

$$v = 0 \quad \text{at} \quad r = 0,$$

$$h = 0 \quad \text{at} \quad r = r_o$$

For cold core rings, the boundary conditions are

$$v \to 0 \quad \text{as} \quad r \to \infty$$

$$h = 0 \text{ at} \quad r = r_o$$

and vary ζ . Eq. (2.41) is a nonlinear eigenvalue equation for ε and should be solved numerically using a Runge-Kutta method. The solutions of warm and cold rings were plotted in the same reference (Flierl, 1979, Fig. 6 and Fig. 10). One may read the maximum current speed from these figures. Refering to remote sensing data, it is possible to measure r_o from a cloud-free satellite image. The maximum tangential speed at $r = r_o$ can be estimated from those figures.

Refering to the second approximation, a particle moves in a curved path in such a way that the centripetal acceleration due to the deflecting force of the earth's rotation is balanced by the centrifugal force of the path curvature, or $f u_\theta = u_\theta^2/r$, where U_θ is the velocity of the particle relative to the earth. Inerital motion on the earth is necessarily anticyclonic, and closes a path having a radius $r = U_\theta/f$ in the period of one-half pendulum day. Since the Coriolis parameter f is a function of latitude, the path of a body in inertial motion is circular when it is symmetrical

with respect to the pole or when it is projected on the equatorial plane of the earth where f is constant; that is, where f is independent of the radial distance from the axis of rotation. The time needed to complete a full path around the circle of inertia is called the inertia period, $T_p = \frac{2\pi}{f} = \frac{2\pi r}{u_\theta} = \frac{\pi}{\Omega \sin\phi}$ Thus, the inertia period depends only on geographical latitude.

$2\pi/\Omega$ represents a sidereal day, which is about four minutes shorter than a solar day. The inertia period is also known as "half a pendulum day" since it is half the period of revolution of a Foucault's pendulum. Thus, at the poles, T_p is approximately 12 hours, at latitude 30°, T_p is approximately 24 hours, and at the equator T_p is infinite. For mid-latitude around 45°, f equals 10^{-4} approximately. At this latitude a current of 10 cm/sec the radius of the inertia circle is approximately 1 km and inertia period is approximately 17.4 h; and a current of 100 cm/sec the radius of inertia circle is approximately 10 km, and with inertia period of 17-18 hr. Motion in an inertia circle has been shown to be quite real in natural situations where there is a sudden impulse which generates fluid motion and allows the system to coast without further interference. The classical example of inertia currents with a translatory motion superimposed was obtained in the Baltic Sea by Gustafson and Kullenberg. Neumann (1968) stated that the period of oscillation is about 14 hours which agrees well with the theoretical inertia period of 14 hours and 8 minutes in the latitude of observation. Some other recent examples were observed in the deep sea at latitude of about 31.5°N and 143°E, a distance of 300 K m from Torishima (Nan'niti et. al., 1964).

In regard to cyclostrophic motion, there is an approximation of small scale motion where the Rossby number, which is the ratio of inertial force to Coriolis force, is very large. In this case, U_θ^2/r becomes much greater than the term $f\,U_\theta$, and the Coriolis acceleration may be neglected. Pure cyclostrophic motion can be cyclonic or anticyclonic depending on the initial rotation but the pressure gradient must always be positive. In equatorial regions, cyclostrophic motion can be expected to occur more frequently at higher latitudes, because f is zero or approximately zero in that area. For example, in mid-latitude, $f \approx 10^{-4}$ and in lower latitudes around 4° or 5°, $f \approx 10^{-5}$, when a U_θ = 100 cm/sec, r will be 10 km for mid-latitude and 100 km for lower latitudes at 4° or 5°, approximately.

2.3 Deflected plume from inlets and bays.

Deflected plume trajectory is also a good tracer for determining cross current, because the out-flowing plumes generally have their special surface or near surface characteristics that can be sensed quite clearly in a cloud-free image. These special characteristics can be the sea surface temperature anomaly, the sea surface roughness, and/or the sediment anomaly between the plume jet and the ambient fluid. The sea surface temperature anomaly can be the result of the discharge of heated water from a power plant. Typical condenser water flow rate is about 1500 ft^3/sec (675×10^3 gal/min). This results in about 12°F for nuclear plants (Lee and Sengupta, 1978). If the heated water is discharged finally to the ocean, it will affect the sea tempera-

ture to some extent and the temperature anomaly on the sea surface can be sensed by an infrared image. Similarly, the outflowing plumes always carry a lot of suspended sediments, which are also good tracers for the satellite visible images. When there is a cross current flowing near or far field outside the mouth of the discharge, the discharged flow becomes deflected (if the Coriolis parameter can be neglected). There are two processes which are considered the cases of a turbulent deflected flow: the entrainment of the lateral momentum of the longshore current and a net pressure force caused by eddying of the ambient fluid in the lee of the jet and the distortion of the jet boundaries. If the bottom friction force can not be neglected, another bottom drag should also be considered.

Many mathematical models have been desired to analyze the characteristics of a surface plume. An excellent reveiw and evaluation of 40 surface plume models has been presented by Dunn et. al., (1975). Some of the models are described hereafter. Edinger and Polk (1969) present analytical solutions which assume that the heated discharge is a point source of heat at the water surface on the boundary of a uniform stream which is infinitely wide and deep. Carter (1969) treats the case of a heated discharge from a channel into an infinitely long and wide basin with uniform depth as the channel and with a cross current that is flowing at right angles to the discharge. Strazisar and Prahl (1973) modify Carter's model with the effects of bottom friction for non-buoyant jet entering perpendicular to a crossflow of constant depth that equals to that of the jet. Hoopes (1968) treats the problem similarly to Carter and assumes that

there is no vertical entrainment and that the constant depth jet is discharged into an infinitely wide and deep basin. These models, solved by the method of integral, have been widely used since they have some predictive capability and are computed more economically that numerical models (Wada, 1968; Prych, 1973; Shirazi and David, 1974; Stolzenbach and Harleman, 1971). Numerical models are becoming more and more popular because high speed computers are available and numerical techniques are developed. More importantly, the three-dimensional nature of buoyant plumes and also time dependent behavior with time varying boundary conditions can be accurately simulated (Sengupta and Lick, 1974; Waldrop and Farmer, 1974; Lee and Sengupta, 1978).

In order to apply for the remote sensing data, I would like to choose a popular model that is able to show the relation between the cross current to the outflowing deflected plume trajector. More perfect models are still available; however, they can be solved only by numerical techniques (refer to previous section). This model was developed by Stolzenbach and Harleman (1971) and discusses two parts: one is non-buoyant surface jets; the other is buoyant jet. Non-buoyant surface jets are considered with a discharge of water horizontally from a rectangular open channel into a large body of water at the same temperature as the discharge. No bottom slope and no ambient crossflow is considered. Buoyant jets are considered with the horizontal surface discharge of water from a rectangular open channel into a large body of water. The temperature of the discharge is greater than that of the ambient water. There is no bottom slope and no

ambient cross current to be considered first. These effects will be included later.

The two coordinate systems used in the development of the model equations is shown in Fig. 2.2. The $\tilde{x}$, $\tilde{y}$, $\tilde{z}$ system is a rectangular Cartesian coordinate system oriented along the centerline of the jet so that $\tilde{x}$ direction is outward and tangential to a point at centerline, $\tilde{y}$ direction is perpendicular to $\tilde{x}$ and toward right of $\tilde{x}$, and $\tilde{z}$ is vertically upward. The second system, designated x,y,z is a rectangular Cartesian system centered at the center of the outlet of the channel so that x is offshore, y is shore parallel and z is upward. The angle between the x and y axis is θ , the jet being discharged with an initial angle θ_o . The cross current velocity , V , may be a function of x but not y . These two systems are related by the equations

$$\frac{dx}{d\tilde{x}} = \sin\theta$$

$$\frac{dy}{d\tilde{x}} = \cos\theta$$

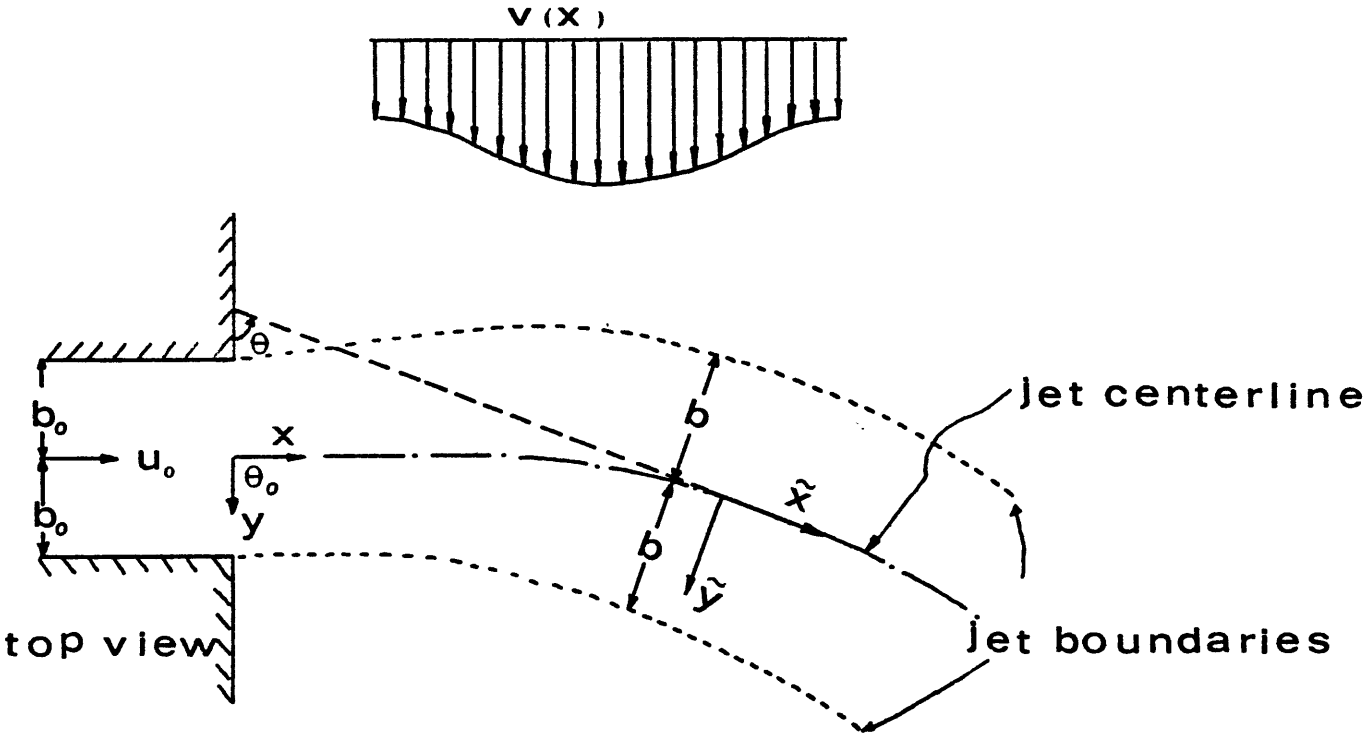

Fig. 2.2 - Characteristics of a Deflected Plume Jet
(after Stolzenbach and Harleman, 1971)

Motivated by experimental results from non-buoyant jet theory, Stolzenbach and Harleman (1971) divide the jet conceptually into four separate regions, as shown in Fig. 2.3. The physical characteristics of the four regions are assumed as:

Region 1: An unsheared central core of half-width s and depth r.

Region 2: A vertically sheared region of thickness h below the core.

Region 3: A horizontally sheared region of width b, laterally adjacent to the core.

Region 4: A region sheared in both directions.

In the unsheared regions, the velocity and temperature profiles are assumed to be uniform, whereas in the sheared regions the profiles are assumed to decay smoothly from their maximum values at the interior edge of the region to zero at the boundary of the jet. The similarity functions for velocity and temperature within the jet are taken as

$$\tilde{u}(\tilde{x},\tilde{y},\tilde{z}) = u_c(x) F_y F_z + V\cos\theta$$
$$\Delta T(\tilde{x},\tilde{y},\tilde{z}) = \Delta T_c(x) T_y(y) T_z(z) \qquad (2.43)$$

where

$$F_y \begin{cases} 1.0 & , \ 0 < y < s \\ f\left(\frac{y-s}{b}\right) & , \ s < y < b \\ 0 & , \ b < y \end{cases}$$

$$T_z \begin{cases} 1.0 & , \ -r < z < \eta \\ f\left(\frac{-z-r}{h}\right) & , \ -h < z < -r \\ 0 & , \ z < -h \end{cases} \quad \text{(surface elevation)}$$

$$T_y \begin{cases} 1.0 & , \ 0 < y < s \\ t\left(\frac{y-s}{b}\right) & , \ s < y < b \\ 0 & , \ b < y \end{cases}$$

$$T_z \begin{cases} 1.0 & , \ -r < z < \eta \\ t\left(\frac{-z-r}{h}\right) & , \ -h < z < -r \\ 0 & , \ z < -h \end{cases} \quad \text{(surface elevation)}$$

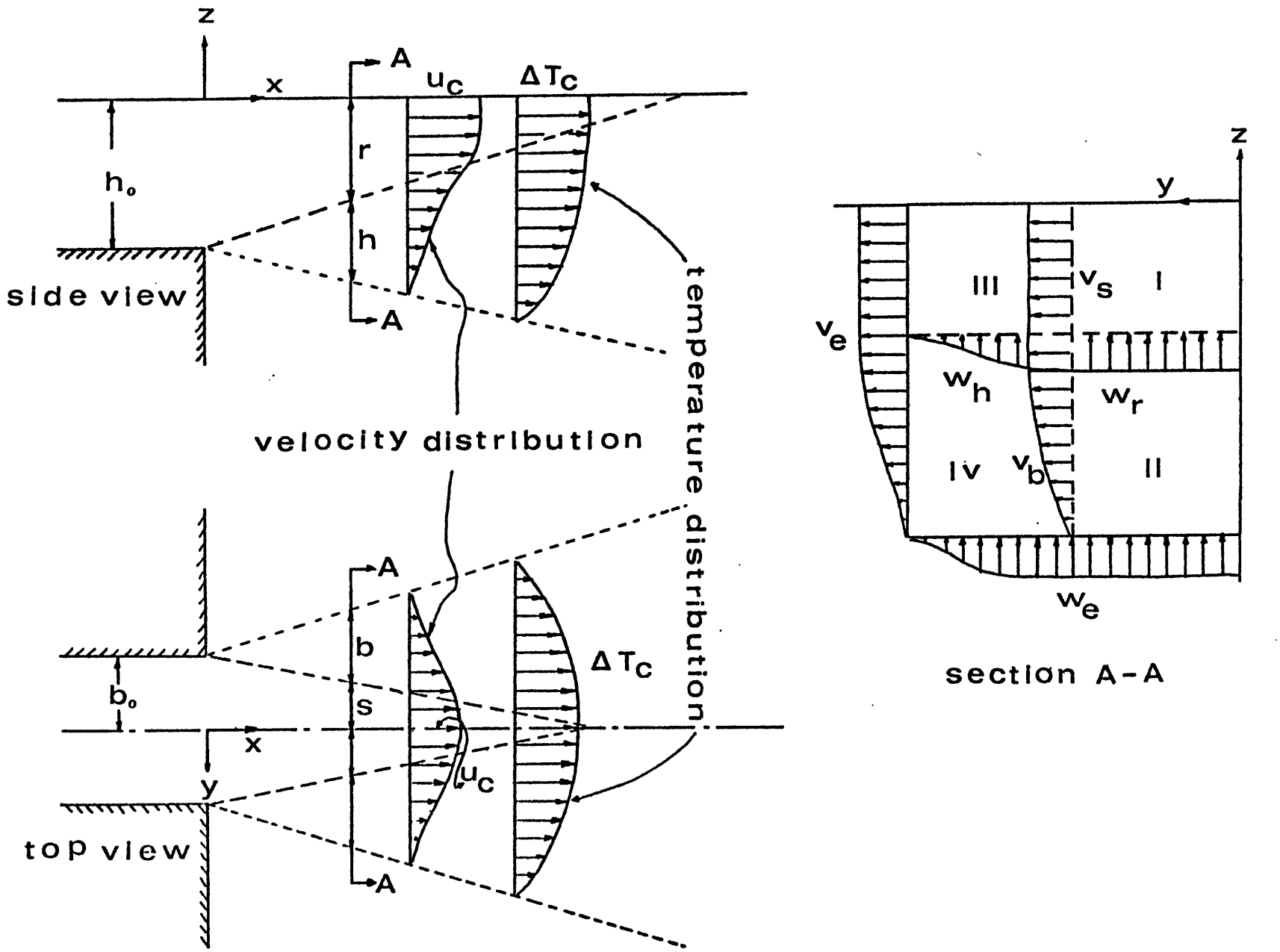

Fig. 2.3 Geometrical characteristics of the plume jet (after Stolzenbach and Harleman, 1971)

and $f(\zeta)=(1-\zeta^{3/2})^2$, $t(\zeta)=\sqrt{f(\zeta)}$ and $\zeta_y = \frac{y-s}{b}$, $\zeta_z = \frac{-z-r}{h}$

The concept of entrainment velocity is very important for this model. A lateral entrainment velocity V_e and a vertical entrainment velocity W_e are assumed to exist on the three submerged sides of the jet, and also further assumed to be proportional to the centerline velocity $U_c(x)$. Thus

$$V_e = \alpha_y u_c(x) \; ; \; w_e = \alpha_z u_c(x) \quad \text{for non-buoyant jet}$$

and

$$V_e = \alpha_y u_c(x) \; ; \; W_e = \alpha_{sz} u_c(x) \quad \text{for buoyant jet} \tag{2.44}$$

where α_y and α_z , α_{sz} are lateral and vertical entrainment coefficients, respectively. It is assumed that for buoyant jets the lateral entrainment is not affected by the buoyancy and that the lateral entrainment coefficient α_y is the same as derived from the non-buoyant jet; however, vertical entrainment is affected by buoyancy and should be corrected. From their studies

$$\alpha_{sz} = \alpha_z \exp\left[-5.0 \; \frac{a\, g\, h \Delta T}{\rho_a u_c^2}\right] \tag{2.45}$$

where a: thermal expansion coefficient

$\Delta T = T - T_a$, temperature rise above ambient in jet. T_a, ambient temperature

ρ_a : the density of the ambient water

and

$$\alpha_y = \begin{cases} -(I_1 - I_2)\,\varepsilon & S > 0 \\ -I_1\,\varepsilon/2 & S = 0 \end{cases}$$

$$\alpha_z = \begin{cases} (I_1 - I_2)\,\varepsilon & r > 0 \\ I_1\,\varepsilon/2 & r = 0 \end{cases}$$

where ε is the spreading rate of a free turbulent region taken to be 0.22 normally.

The equation of jet bending used only for nonzero cross current is derived from the following integral conservation relationship:

$$\frac{d\theta}{d\tilde{x}} \int_0^{S+b} \int_{-r-h}^{0} \tilde{u}^2(\tilde{x}, \tilde{y}, \tilde{z})\, d\tilde{y}\, d\tilde{z} = V \sin\theta \left\{ \int_{-r-h}^{r} V_e\, f\left(\frac{-\tilde{z}-r}{h}\right) d\tilde{z} \right.$$

$$\left. + \int_{-r}^{0} V_e\, d\tilde{z} + \int_0^S w_e\, d\tilde{y} + \int_S^{S+b} w_e f\left(\frac{\tilde{y}-S}{b}\right) dy \right\}$$

The relation of a cylindrical coordinate system is defined

$$R\,d\theta = d\tilde{x}\ ,\quad dR = -dy\ ,\quad R = -\left(\frac{\partial\theta}{\partial\tilde{x}}\right)^{-1}$$

After these integrations are performed, the result is

$$\begin{aligned}&\left[u_c^2(S+bI_2)(r+hI_2) + 2V\cos\theta\, u_c(S+bI_1)(r+hI_1)\right.\\&\left. + V^2\cos^2\theta\,(s+b)(r+h)\right]\frac{d\theta}{d\tilde{x}} - u_c V \sin\theta\left[-\alpha_{sz}(S+bI_1)\right.\\&\left. + \alpha_y(r+hI_1)\right] = 0\end{aligned} \tag{2.46}$$

where

$$I_1 = \int_0^1 f(\zeta)\,d\zeta = \int_0^1 (1-\zeta^{3/2})^2\,d\zeta = 0.4500$$

$$I_2 = \int_0^1 f(\zeta)\,d\zeta = \int_0^1 (1-\zeta^{3/2})^4\,d\zeta = 0.3160$$

U_c, r , S , α_y , α_z are the following values

Initial region $x < \frac{h_o}{\varepsilon I_2}$, $x < \frac{b_o}{\varepsilon I_2}$

$$u_c = u_o$$

$$r = h_o - \varepsilon I_2 x$$

$$s = b_o - \varepsilon I_2 x$$

$$-\alpha_y = \alpha_z = \varepsilon (I_1 - I_2)$$

For $h_o < b_o$, $\frac{h_o}{\varepsilon I_2} < x < \frac{b_o}{\varepsilon I_2}$

$$u_c = u_o \sqrt{\frac{h_o}{x \varepsilon I_2}}$$

$$r = 0$$

$$s = b_o - \varepsilon I_2 x$$

$$\alpha_y = -\varepsilon (I_1 - I_2)$$

$$\alpha_z = \frac{I_1 \varepsilon}{2}$$

For $b_o < h_o$, $\frac{b_o}{\varepsilon I_2} < x < \frac{h_o}{\varepsilon I_2}$

$$u_c = u_o \sqrt{\frac{b_o}{x \varepsilon I_2}}$$

$$s = 0$$

$$r = h_o - \varepsilon I_2 x$$

$$\alpha_y = -I_1 \varepsilon / 2$$

$$\alpha_z = \varepsilon (I_1 - I_2)$$

For $x > b_o / \varepsilon I_2$, $x > h_o / \varepsilon I_2$

$$u_c = u_o \frac{\sqrt{h_o b_o}}{x \varepsilon I_2}$$

$$r = s = o$$

$$- \alpha_y = \alpha_z = \frac{I_1 \varepsilon}{2}$$

and

$$\alpha_{sz} = \alpha_z \exp\left[- 5.0 \frac{a g \Delta T_c h}{\rho_a u_c^2}\right], \quad \alpha_{sz} \simeq \alpha_z \quad \text{as } \Delta T_c \simeq o$$

$$\varepsilon = 0.22$$

Furthermore, it is possible to measure the figures of b , b_o , θ , θ_o and the R from a satellite image using the MCIDAS system and the cross current at that position can be calculated from Eq (2.46). Dunn et. al. (1975) criticized this model as: "The bending only due to entrainment. Furthermore, the model does not allow external forces, such as wind stress acting at the surface or the drag of ambient current, to bend the jet. Instead only the entrainment of ambient momentum is considered." However, it is thought that momentum entrainment is the major component of bending even within the integral models that allow the drag force.

The sediments discharged by a river occasionally are transported and dispersed along the coast to considerable distances from the river mouth due to the cross current impinging on the coastal waters

near deltas. In addition to the outflowing plume described before, that can be shown in the satellite images, the accumulated sediments on the ocean floor can sometimes be "seen" from an image (e.g., Landsat, Channel 4). In this case, the trajectory and the width of the sediment sitting that represents the average sedimentary transport can be traced approximately from this image. The average cross-current velocity can also be calculated from Eq. (2.46). Sometimes a wave-like suspended sedimentary distribution appears on an image; this sediment transport can be mainly due to M_2 tide. The sediment is transported out of the sea and shifted to the direction of cross-current during low tide period; no sediment is transported out of the sea during high tide period. The wavelength of the suspended sediment can be measured from MCIDAS system and the average period of M_2 tide is also known. The transported speed which is approximately equal to the cross current speed can be estimated.

3. SOME CASE STUDIES

3.1 Methodology

In order to varify the approaches presented in the previous section, we present the following three case studies: to estimate the propagation of the Gulf Stream, the tangential speeds for Gulf Stream eddies and the cross-current off Brazos Santiago Entrance channel. Each case follows the four steps of study: to study the regional oceanographic data; to study the satellite images; to apply the approaches; and to compare the results.

To study the oceanographic data, it is practical to review papers existing in the oceanographic literature. From this study, we will understand more thoroughly the ocean dynamics and the representative oceanographic data of this area. These representative oceanographic data can be used either as parts of the input of the approach or as the velocity ground truth to be compared later with the results.

To study the satellite images is to varify the existing satellite images either from the MCIDAS system or from the Landsat MSS images. Then those images which can possibly provide us with better information for our studies will be interpreted in detail, either through the MCIDAS system or through visual interpretation. The MCIDAS system will enhance and amplify the interesting parts of an image, as well as measure the sea surface features, such as the radius of a core ring, the wavelength of a meander, the distance from a reference position and the location of any particular point. These data are used as parts of the input, together with some other representative data

from step one, to the approaches suggested in Section 2. This is the third step of the study. The estimated velocities are only compared with the representative velocities of that region due to the inavailibility of the ground truth data. A general discussion will be given at the end of this study to examine the possible reasons that lead to incorrect results.

3.2 Propagation of the Gulf Stream

In order to estimate the propagation speed of the Gulf Stream, using the methods in Section 2.1, we have to do some research on the average oceanographic data of this region, such as depth of the thermocline, length scale, velocity scale bottom slope, etc., in addition to those wavelengths of the meanders that can be measured directly from the cloud-free images. These kinds of data, of course, will change from place to place; however, my purpose is to search the existing literature for more representative data for the Gulf Stream.

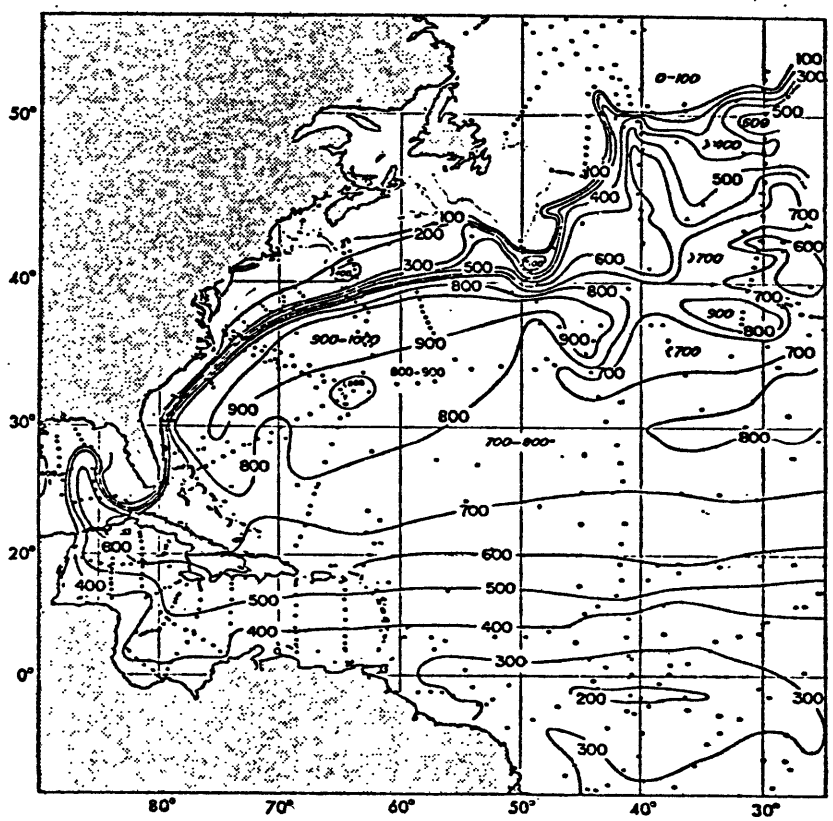

Fig. 3.1 Chart showing the depth of the 10° isotherm in the western North Atlantic (after Iselin, 1936).

The depth of the main thermocline, which is always regarded as the thickness of the upper layer of a two-layer instability model, is usually defined as the depth of the 10°C isotherm. In the western North Atlantic, a chart (see Fig. 3.1) showing the depth of the 10°C isotherm is presented by Iselin (1936). This temperature, which represents the middle of the main thermocline, also meets the definition of mid-thermocline* classified by Worthington (1976). Referring to this chart, the 10°C isothermal surface reaches a maximum depth between 800 and 900 meters under the Sargass Sea, and may often rise to 200 meters in the slope water, and practically reaches the surface in the vicinity of Nova Scotia and Newfoundland. The average value is around 500 m under the main flow of the Gulf Stream. Fuglister (1963) also presents a chart showing 10°C isotherm depth similar to that of Iselin. More detailed profiles at any particular position can be referred to the Oceanographic Atlas at that area, for example, the Atlantic Ocean Atlas by Fuglister (1960). However, 500 m can be a good representative value of 10°C isotherm in the main stream.

---

*Worthington (1976) defines the mid-thermocline of the North Atlantic as the water temperatures between 7 and 12°C.

Regarding the length scale of the Gulf Stream, we may obtain an idea from the Gulf Stream width. Then the measurement of the Stream width will depend on the definition of the Gulf Stream boundaries. Fuglister and Worthington (1951) suggested that the northern edge of the Gulf Stream is the line along which the horizontal pressure gradient is zero. Stommel (1965) defines that the Gulf Stream is a band of swift current stretching from the continental shelf off Cape Hatteras* to the 50th meridian of longitude, south of the Grand Banks of Newfoundland, with a pronounced pressure gradient between the warm, highly saline water to the south, and the colder, fresher water to the north. Using this definition then, he also defines the inner and outer limits or edges of the Gulf Stream to be as the points where the pressure gradient becomes zero. These points, as he explains, can be obtained from the cross current pressure gradients, that are calculated from the deep, closely spaced temperature and salinity data. Another method to define the northern surface boundary of the Gulf Stream for the width estimation is the location

---

*Iselin (1936, p. 73-75) defined the entire set of western currents to be the Gulf Stream System and the Florida Current. The Gulf Stream was retained for the section of the current between Cape Hateras and the tail of the Grand Banks. The part between Tortugas, in the Florida Straits, to Cape Hatteras was not included in Gulf Stream System. But Stommel (1965) prefers to use the term of Gulf Stream System in a more general sense than that proposed by Iselin; and restricts the use of the Florida Current within the Florida Straits.

of the 15°C/200 m isotherm (Fuglister and Voorhis, 1965), which is about 15 km away from its actual measured surface boundary. As early as 1936, Iselin already had pointed out that the gradient zone slopes downward at an angle on the order of one-half degree. This will make the surface gradient about 20 km north off the subsurface gradient. In a study of the relation between surface and subsurface gradients across the northern edge of the Gulf Stream, Strack (1953) also found relatively small horizontal displacements of about 18 km between the surface and the subsurface gradients from November to May. This result suggests that a surface gradient is a good indicator of the position of the northern edge of the Gulf Stream. Remote sensors nowadays can also locate the surface boundary of the Gulf Stream. Many investigators define the maximum surface thermal gradient as the northern thermal boundary of the Gulf stream (eg. Wilkerson, 1967; Rao, et. al., 1971; Maul and Hansen, 1972). From an observation of the Gulf Stream surface front structure by ship, aircraft and satellite, Hansen and Maul (1970) found that the surface boundary obtained from IR images is an average 14.5 km north of the 15°C/200 m isotherm. This result is in good agreement with those of Iselin, Fuglister and Voorhis, and Strack. Unfortunately, the outer boundary of the Stream generally can not be "seen" as clearly in images (IR or visible) as that of the inner side. These studies suggest that the surface boundaries of the Gulf Stream are also good for us to define the Gulf Stream, although they still have about 10% of the position error to the subsurface 15°C/200 m isotherm. Referring to today's oceanographic literature, we don't have much difficulty finding

the data of the Stream width, although most of the authors did not mention very clearly how they measured it. Stommel (1948) says the width of the region of strong northward current (I think he means the Gulf Stream) is less than 100 km; Munk (1950) suggests 200 km and 250 km as typical values for the widths of the western current and counter-currents, respectively; Morgan (1956) finds the Stream width to be 150 km; Pickard (1975) estimates the Gulf Stream width, from temperature and salinity profiles of the Chesapeake Bay to Bermuda section performed in August/September 1932 by Iselin, to be 120 km. I personally estimate the Stream width, from the sharpest points of the temperature and salinity gradients in both sides of two larger-scaled temperature and salinity profiles in the Atlantic Ocean Atlas (Fuglister, 1960), to be roughly 200 km at 32°N and 120 km at 36°N. Overviewing the above-mentioned data, I would prefer to take 120 km as a reasonable length scale over the Gulf Stream System.

The velocity scale of the Gulf Stream can be roughly estimated from the surface current measurements available. Earlier estimation by dynamic computation shows that the surface velocity ranges from 100 to 120 cm/sec (2-2.4 knots) (Iselin, 1936). Later, using the Loran system and the bathythermograph to track the path, Iselin and Fuglister (1948) measured the surface velocities to be often as high as 200 — 250 cm/sec (4-5 knots), which is almost twice of the earlier estimation. Iselin and Fuglister (1948) also pointed out that the previous data should be less than the real ones because the stations used for the computations were too far apart to calculate the true slopes of the isobaric surface. Worthington (1954) calculated the

geostrophic current velocity from the closely spaced section showing that the surface velocities are 180 cm/sec at station 4857 and 200 cm/sec at station 4859. Sometimes the average velocity of a current can also be calculated from its mass flux. The mass flux of the Gulf Stream has been estimated to be the range of 100-150 sv. south of Cape Cod (Fuglister, 1963; Warren and Volkmann, 1968; Knauss, 1969). However, the net wind stress driven transport is only 38 sv., because most of the transport in the Gulf Stream is recirculated in the western North Atlantic (Stommel,et. al., 1978). Suppose that no interior dissipation for the wind energy and widths of boundary current of 80-150 km and a depth of 500 m; these energy and mass fluxes require a mean speed of 100 cm/sec $\sim$ 50 cm/sec in the western boundary current. Von Arx (1962) pointed out that "the velocity of the Gulf Stream is usually greatest at or very near the surface, where it may range from 100 cm/sec to values approaching 300 cm/sec. Unless local winds have mixed the surface momentum downward, the velocity will decrease regularly with depth to about the 500 meter level," and "reach values in the order 1 to 10 cm/sec in depths between the 1500- to 2000-meter levels." The direct measurements of the Gulf Stream velocities are scarce. On a six-day cruise of the Bear and the Caryn in July 1952, Malkus measured the vertical velocity profiles by the Malkus barhypitotmeter and checked by Watson propeller type meter. The results show that the surface current speeds reach 4.5 - 5 knots and decrease gradually with the depths, with the highest speed particularly at the edge of the warm core, decreasing to approximately one knot at 200 m, and approaching zero at 800 m. (Fig. 3.2). Justifying from the above-mentioned

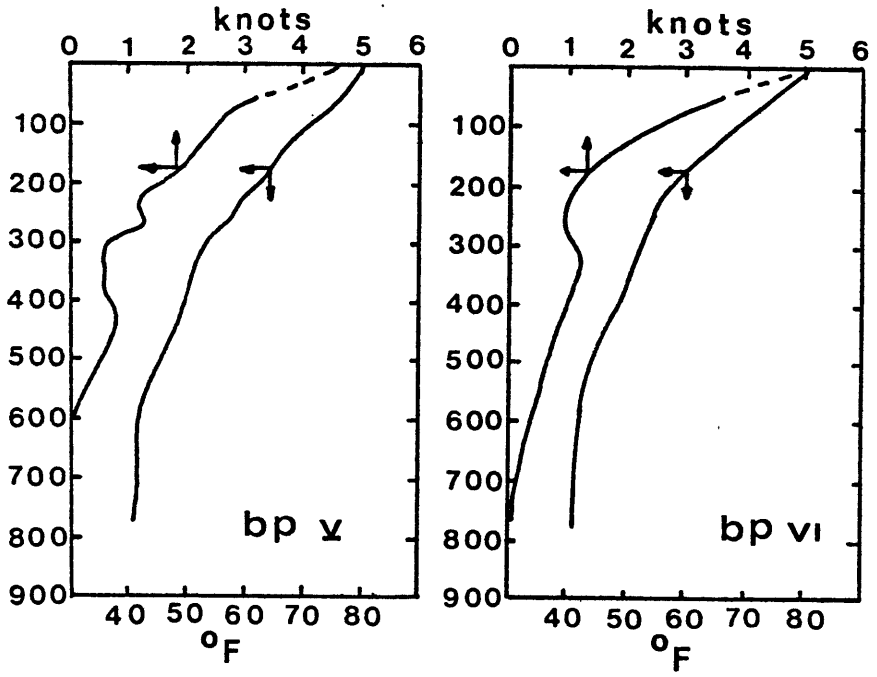

Fig. 3.2 Bathypitotmeter measurements of current at two stations in the Gulf Stream. Both of bathypitometer soundings, BP V and BP VI, were made in the left-hand edge of the warm core, where the highest velocity was. Obtained by Dr. William Malkus, June 1952 (after Stommel, 1965).

data, we can choose the surface current velocity scale to be in the order of 200 cm/sec (4 knots), and that of the bottom layer to be in the order of 10 cm/sec (0.2 knot).

The bottom slopes in the coastal area very from place to place. They are the steepest near Cape Hatteras, the less off Florida, and the least off Cape Cod. From the Mercartor Maps of NOAA #11009 and #13003 we estimate the average slopes of these three continental slopes to be 1.17×10^{-2}, 7.8×10^{-3} and 1.8×10^{-3}, respectively.

From the above-mentioned studies, the more representative data of the Gulf Stream chosen for our analyses are:

h_1 or h_o = 500 m (depth scale of the upper layer)

h_2 = 3000 m (depth scale of the lower layer)

L = 150 km (length scale)

U = 200 cm/sec (174 km/day) (velocity scale)

f_o = 10^{-4} rad/s

α = -1.17×10^{-2} at the Cape Hatteras (bottom slope)

$g' = g \Delta\rho/\rho$ = 1 cm/s^2

Using these data scales, the nondimensional parameters of F_1, F_2, T can be calculated as

$$F_1 = \frac{f_o^2 L^2}{g\frac{\Delta\rho}{\rho} h_1} = \frac{(10^{-4})^2 (120\times10^3)^2}{0.01 \times 500} = 29$$

$$F_2 = \frac{f_o^2 L^2}{g\frac{\Delta\rho}{\rho} h_2} = \frac{(10^{-4})^2 (120\times10^3)^2}{0.01 \times 2000} = 7$$

$$T = \frac{\alpha f_o L^2}{h_2 U} = \frac{-1.17\times10^{-2}\times10^{-4}\times(120\times10^3)^2}{2000 \times 0.2} = -42$$

We can supply these data to the two-layer models in Section (2.1.2). The most suitable model applied to the Gulf Stream System before reaching Cape Hatteras is a two-layer flow without zonal flow, i.e., case III. We choose two sets of typical nondimensional mean velocities to represent the layers of the Gulf Stream: $V_1 = 1$, $V_2 = \pm 0.2$ and $V_1 = 0.9$, $V_2 = \pm 0.1$. V_1 and V_2 stand for the nondimensional mean velocities in the upper and lower layers, respectively. $V_1 = 1$ corresponds to a northward dimensional flow of 173 km/day (200 cm/sec). First I check which wavelength ranges of the Gulf Stream meanders off Cape Hatteras are the most unstable; and then if we have some meander wavelengths obtained from an image, we may check their instabilities

and estimate the approximate phase speeds of these conditions and also their mean velocity ranges in either layer. The formula to be applied for this analysis is

$$a\sigma^2 + b\sigma + d = 0 \tag{2.21}$$

where

$$a = K^2 (K^2 + F_1 + F_2)$$

$$b = -l [a (V_1 + V_2) + K^2 (V_1 - V_2)(F_2 - F_1) - T (K^2 + F_1)$$

$$d = l^2 [a V_1 V_2 + K^2 (V_1 - V_2)(V_1 F_2 - V_2 F_1) - T (K^2 V_1 + F_1 V_2)]$$

The results are shown in Figs. 3.3 and 3.4 , and summarized in Table 3.1 . Figs. 3.3 and 3.4 shows that the wavelengths at which the flow is in baroclinically unstable are from 88 to 103 km with the fastest growing rate at 94 km for $V_1 = 0.9$, $V_2 = 0.1$; from 91 km to 113 km with the fastest growing rate at 100 km for $V_1 = 0.9$, $V_2 = -0.1$; from 85 to 100 km with the fastest growing rate at 94 km for $V_1 = 1$, $V_2 = 0.2$ and from 97 km to 137 km with the fastest growing rate at 107 km for $V_1 = 1$, $V_2 = -0.2$. The phase speeds of the most unstable waves are 117.5 km/day, 100 km/day, 104.4 km/day and 82.3 km/day, respectively.

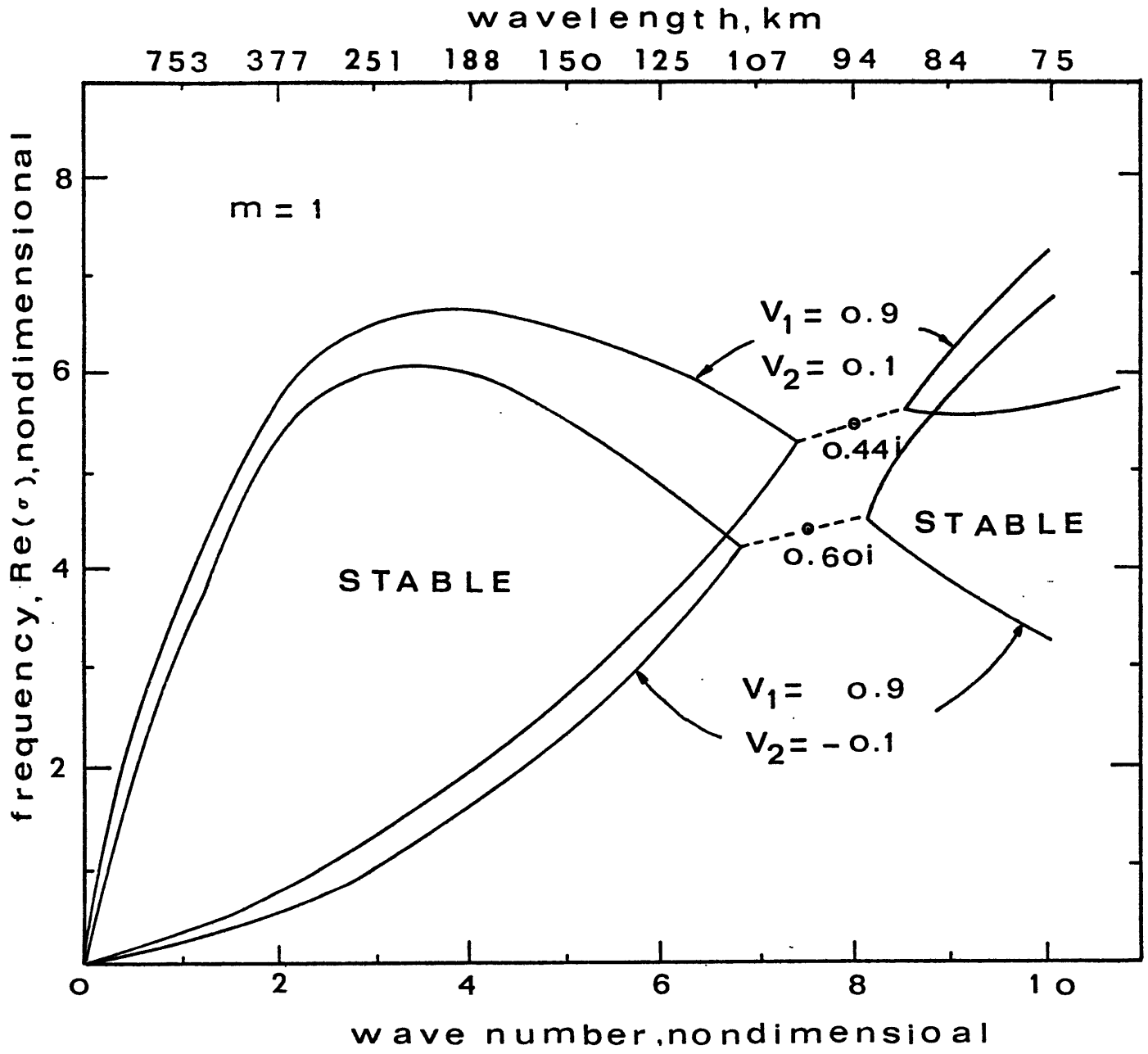

Fig. 3.3 Dispersion relation of the Gulf Stream off Cape Hatteras for mode m=1 , with V_1=1.0 ; V_2= $\pm$0.1.

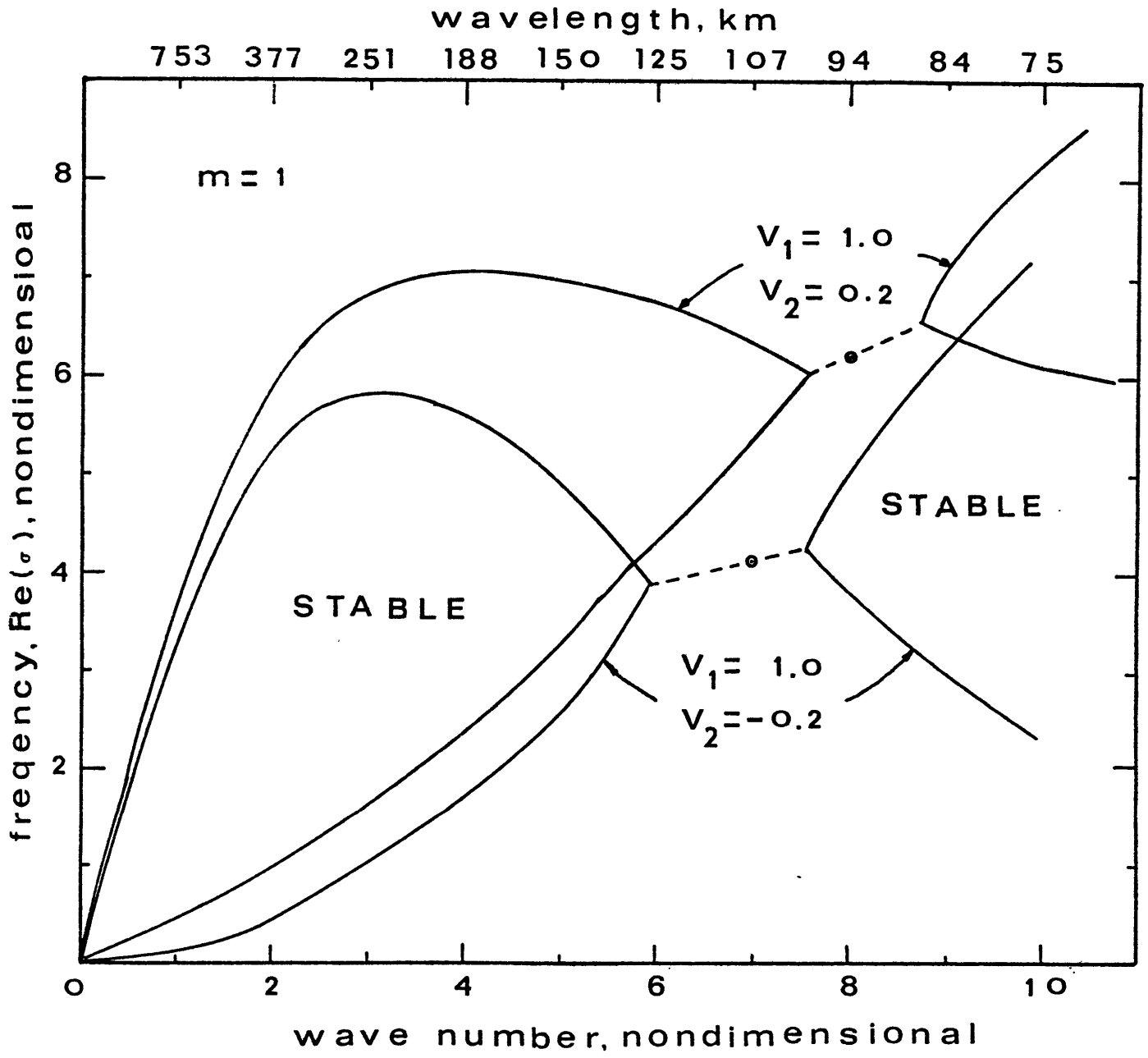

Fig. 3.4 Dispersion relation of the Gulf Stream off Cape Hatteras for mode m=1 , with V_1=1.0 ; V_2= $\pm$0.2.

Table 3.1 Summary of the Unstable Wave Properties for m=1

V_1 , V_2	Unstable Wavelength Range, Km	Most Unstable Waves		
		Period, days	Wavelength, km	phase speed km,day
0.9,0.1	88-103	0.8	94	117.5 (136cm/sec)
0.9,-0.1	91-113	1.0	100	100.0 (116cm/sec)
1.0,0.2	85-100	0.9	94	104.4 (120cm/sec)
1.0,-0.2	97-137	1.3	107	82.3 (95cm/sec)

A TIROS N VHRR image was taken on March 23, 1979 as shown in Fig. 3.5. With the assistance of the MCIDAS System, we interpret this image and measure the wavelength of a Gulf Stream meander at the inner boundary off Cape Hatteras between 35 and 35°30'N to be 110 km approximately. The distance measurement error from the equipment is quite small. In addition to some man-made error, we estimate this measured error should not exceed 10%. This wavelength allows us to estimate the wave phase speed both for the stable condition and for the baroclinically unstable case. Except for the measured wavelength, λ , is 110 km, the other representative data for this area, as studied before, to be

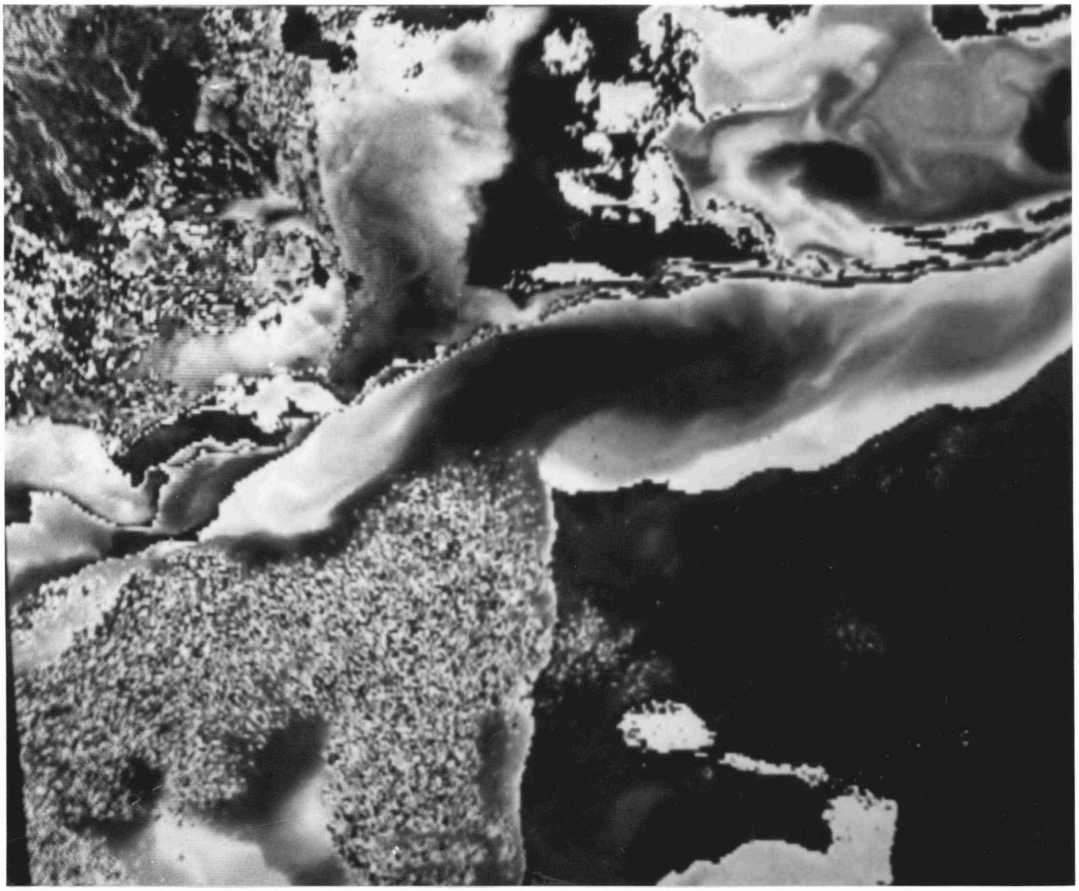

Fig. 3.5 TIROS VHRR image showing the Gulf Stream meander on March 23, 1979.

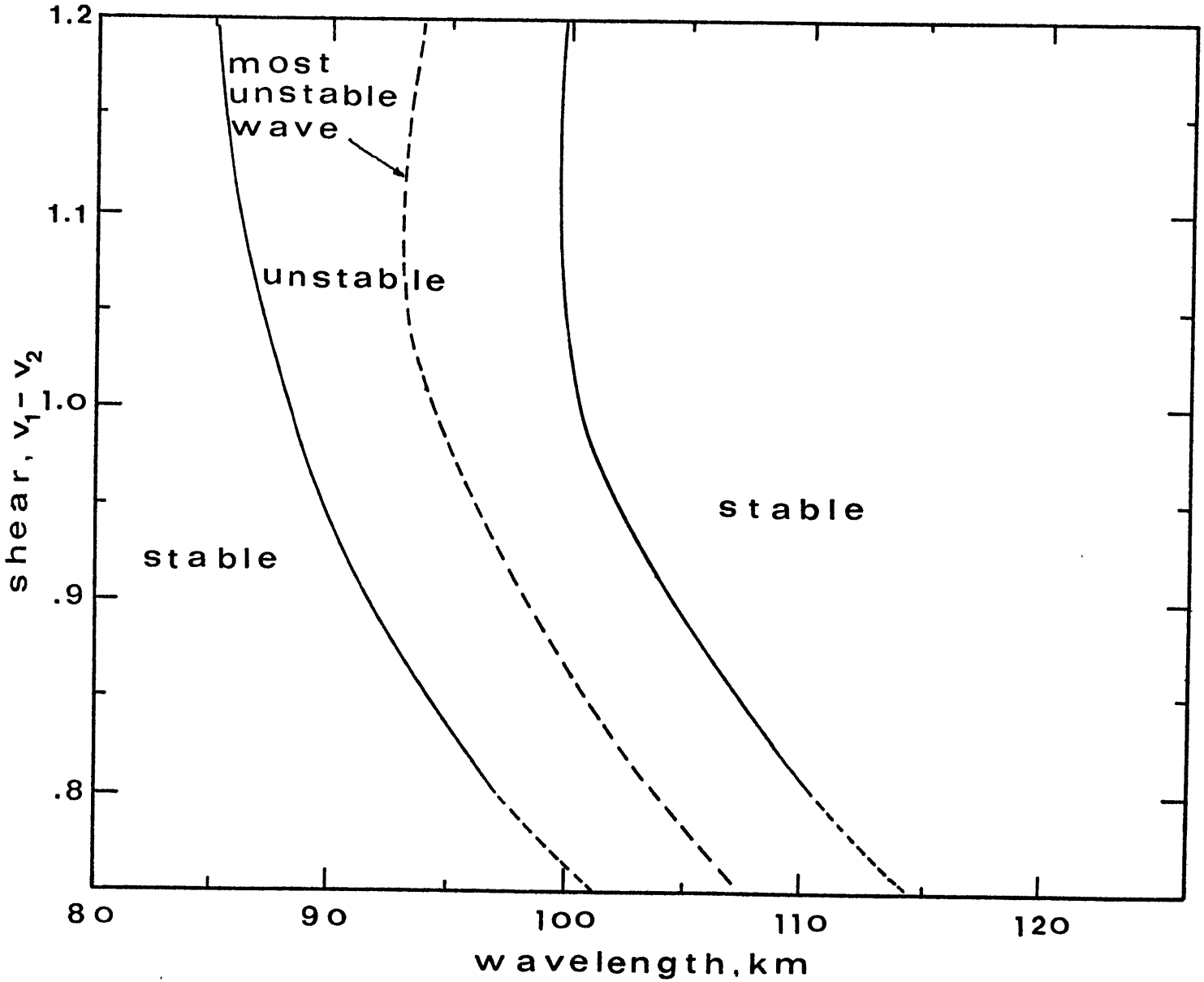

Fig. 3.6. Relations between wavelength and shear of the Gulf Stream off Cap Hatteras

$g' = g\frac{\Delta\rho}{\rho}$ (reduced gravity) $\approx$ 1 cm/sec^2

$f \simeq 10^{-4}$/sec

h_o or h_1 (upper layer depth) = 500 m

$c = \sqrt{g'h_o}$ = 2.24 m/sec

Assume the meander to be in a stable condition and to be wide enough as explained in Section (2.1.1). The phase speed is

$$C_y = \frac{\sigma}{l} = \frac{c^3 l^2}{6f^2} = \frac{(2.24)^3(2\pi)^2}{6\times(10^{-4})^2(110\times10^3)^2} = 61 \text{ cm/sec (1.2 knots)}$$

This phase speed is much less than the current speeds as mentioned before. However, in view of the baroclinically unstable case, this wavelength in practice stays near that of the most unstable wave. Fig. 3.6 shows the relation between the wavelength and shear of the main flow, while also showing the properties of the most unstable waves. Referring to Fig. 3.6 this wavelength (110 km) has a maximum nondimensional shear of 0.8. When the lower layer is at rest, this shear is correspondent to a upper layer mean flow velocity of 160 cm/sec (3.2 knots) when the velocity scale 200 cm/sec is used. As the field measurements show, the lower layer of the Gulf Stream also has a mean flow of the order of 10 cm/day, which is about 10% of that of the upper layer, and the direction is practically the same as the upper layer. That means $V_1 = 0.725$; $V_2 = 0.075$. These

nondimensional mean flows correspond to an upper layer mean flow velocity of 145 cm/sec (2.9 knots) and a lower layer mean flow velocity of 15 cm/sec. Unfortunately, the ground truth is not available; however, these estimated speeds are in good agreement with previous field measurements by Iselin (1936) and Seiwell (1939) by roughly +7 $\sim$ +15%, and less than those calculated by Worthington (1954) by roughly 20%. But one must remember that those calculated and measured data are the maximum surface velocities and should be higher than the mean velocities in principle.

3.3 Tangential Speeds for Gulf Stream Eddies

Some typical data discussed in Section 3.2 are still applicable for the Gulf Stream eddies. The thermocline depth, h_o , is also of the order of 500 m. In order to estimate the tangential speeds for the Gulf Stream eddies, we choose two TIROS-N VHRR images, which clearly show the Gulf Stream warm rings centered at about 69°W and 39°N, approximately five years apare in time.

The first image (the later one) was taken on March 23, 1979. With the assistance of MCIDAS, we find its center position 39.166°N and 68.862°W, which is located 281 km south-east of Cape Cod. After repeated measurements we find the core ring is almost round with the average radius 66 km (Fig. 3.7). The second one (the earlier image) was taken on May 11, 1975 with the ring centered at 39.040°N and 69.024°W. The average radius is 88.5 km; the shape is round and roughly circular (Fig. 3.8). The location of both rings are very close to that of Ring L found by the RV/KNORR 65 in April 1977; but really can

Fig. 3.7. TIROS-VHRR image showing a Gulf Stream ring centered at 39.166°N and 68.862°W on March 23, 1979.

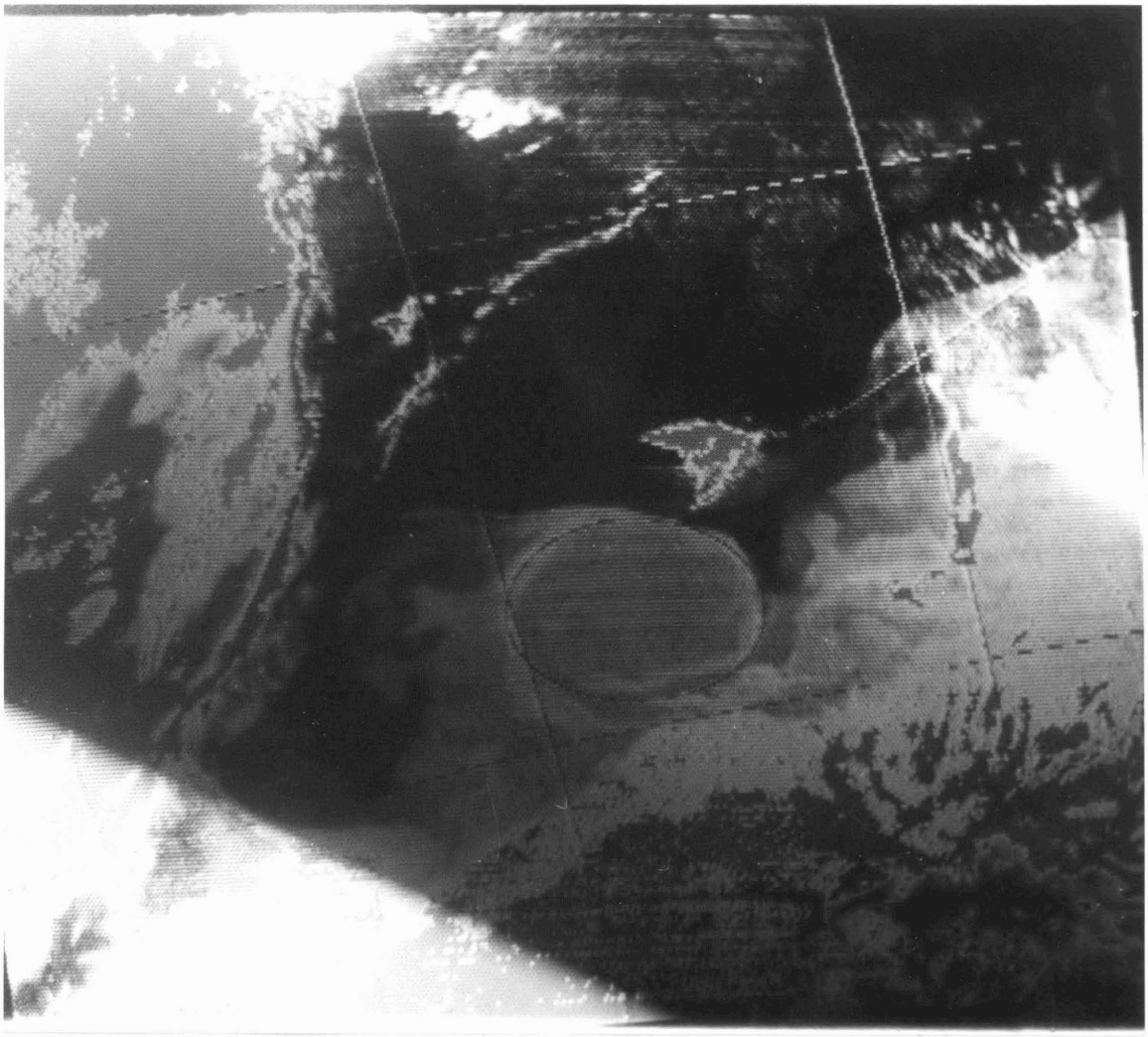

Fig. 3.8. TIROS VHRR image showing a Gulf Stream ring centered at 39.040°N and 69.024°W on May 11, 1975.

not be the same ring because of the short lifetime of a warm core ring in the Gulf Stream. The measured radius is practically equal to r_o , which represents the radius of the ring where the depth of the upper layer, h_1 , vanishes. The radius, r_o , is generally obtained from the field measurements or calculated directly from the known parameters of the initial thermocline depth, h_o , the deformation radius, R , and the volume of anomalous water in the ring. It is very convenient and accurate to measure this radius from an image using the MCIDAS system. The total error, as we estimated before, will not exceed 10%. By knowing r_o , the term $I_o(r_o/R)$ is fixed in Eq. (2.35), then the tangential velocity of a ring and the tangential velocity distribution in the ring can be calculated from the same equation. The data for the first image are:

Location of ring center: 39.166°N, 68.862°W

Satellite and Sensor : TIROS-N VHRR

Date : March 23, 1979

Average radius r_o : 66 km measured from the image

Initial thermocline depth, h_o: 500 m

$R = \sqrt{g'h_o}/f = \sqrt{0.01 \times 500} / 10^{-4} = 22.36$ km

Hence, $r_o/R = 2.95$

Substituting these data to Eq. (2.35), we obtain the tangential velocities of the ring

$$-u_\theta = Rf\,\frac{I_1(r/R)}{I_0(r_0/R)} = 22.36\times10^{-4}\,\frac{I_1(r/22.36)}{I_0(2.95)}$$

$$= 4.763\times10^{-4}\; I_1(r/22.36)\;,\ km/sec$$

$$= 47.63\;\; I_1(r/22.36)\;,\ cm/sec$$

The maximum tangential velocity of this ring is the velocity at $r = r_o$, or

$$-u_{\theta,max} = 47.63\; I_1(66/22.36) = 180.3\ cm/sec$$

The shape of the ring can be obtained from the h equation as Eq. (2.34)

$$h = h_0\left[1 - \frac{I_0(r/R)}{I_0(r_0/R)}\right] = 500\left[1 - \frac{I_0(r/22.36)}{I_0(2.95)}\right]$$

The tangential velocity distribution and the depth (shape) of this ring at different radii are tabulated in Table 3.2 and plotted in Fig. 3.9.

The volume of the anomalous water, decay time scale due to entrainment and due to friction are:

Table 3.2 Tangential Velocity Distribution and Depths at Different Radii, calculated from TIROS image, 3/29/79.

radius, r, km	0	10	20	30	40	50	60	66
$-u_\theta$, cm/sec	0	11	24	40	62	94	142	180
h , m	393	388	371	340	289	212	96	0

$$V = \int_0^{r_o} 2\pi r h \, dr = \pi h_o r_o^2 \left[1 - \frac{2R}{r_o} \frac{I_1(r_o/R)}{I_o(r_o/R)} \right] = 3103 \text{ km}^2$$

$$t_e = V \Big/ \frac{dV}{dt} = \frac{\gamma_v}{\gamma_e} \frac{1}{2\lambda} \frac{f r_o}{g'} = 19 \text{ days for large } r_o/R$$

$$t_f \sim 10^3 \, t_e = 19000 \text{ days (very slow to be neglected compared with } t_e)$$

The data for the second image are:

Location of ring center : 39.040°N, 69.024°W

Satellite and sensor : TIROS VHRR

Date : May 11, 1975

Average radius r_o : 88.5 km, measured from the image

Initial thermocline depth : 500 m

R = 22.36 km

Thus, $r_o/_R = 3.96$. Use the same method as in the first image. We obtain the tangential velocities and the depths at diffent radii for this ring as in Table 3.2

Table 3.2 Tangential Velocity Distribution and Depths at Different Radii ,calculated from TIROS image, 5/11/75

radius, r, km	0	10	20	30	40	50	60	70	80	88.5
$-u_\theta$, cm/sec	0	5	10	17	27	41	61	91	137	178
h , m	454	452	445	431	410	376	326	251	139	0

The relations between the radius and the tangential velocity and between the radius and the depth of this ring are shown on the Fig. 3.9. The volume of the anomalous water, decay time scale due to entrainment and due to friction are 17660 km^3, 26 days and 26000 days. If we apply Flierl's model (1979), the maximum tangential velocities in both cases become much larger. These velocities are estimated to be approximately 260 cm/sec and 230 cm/sec respectively.

The maximum surface velocities in the Gulf Stream are shown in

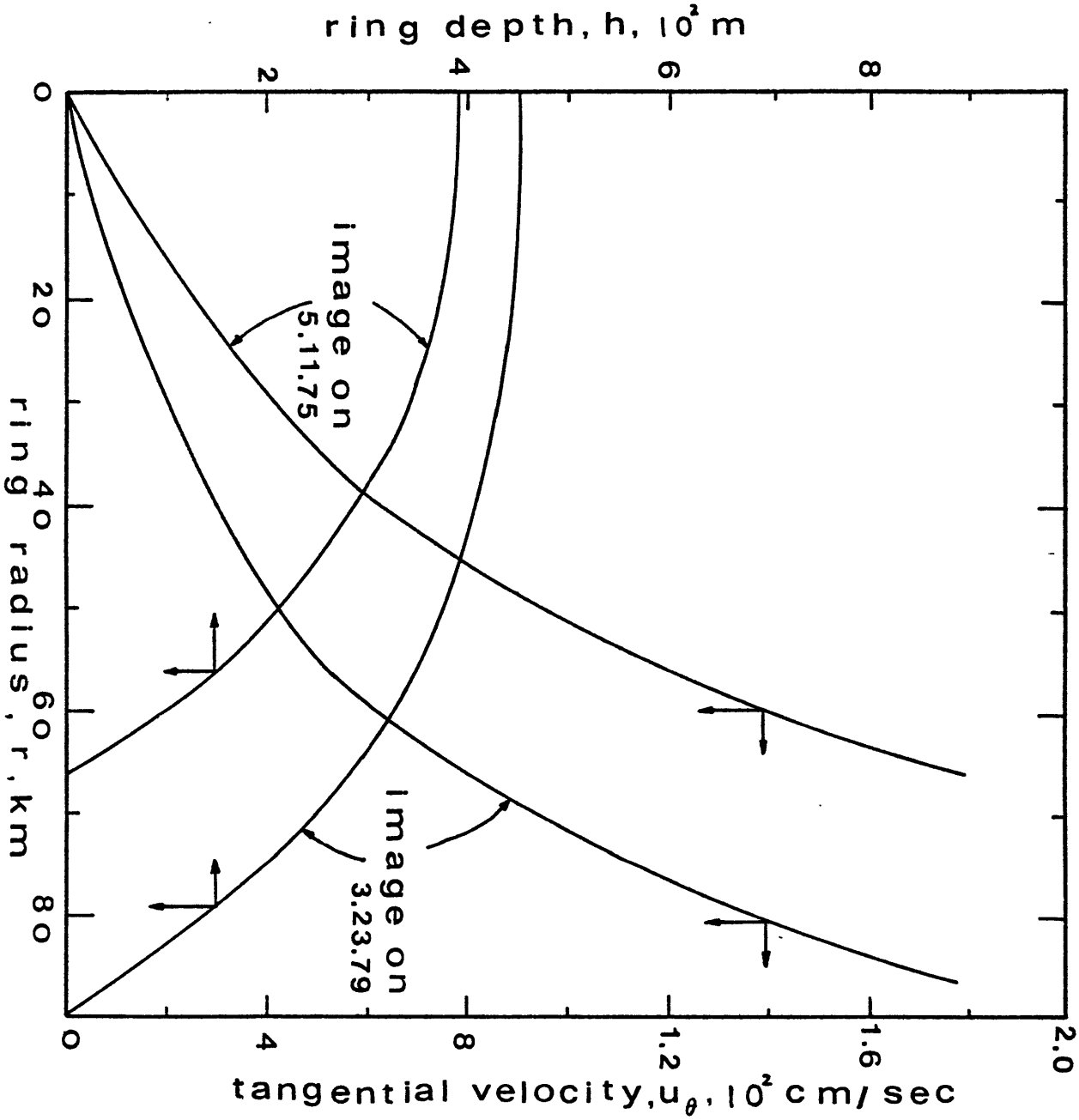

Fig. 3.9 Relations between ring radius and tangential velocity and between ring radius and depth.

Section 3.2. The typical maximum surface velocity is of the order of 200 cm/sec. Our estimations from Csanady's model are averaged to be 179 cm/sec. If we compare this with the geostrophic current velocity calculated by Worthington (1954) of 180 cm/sec at station 4857, this result happens to be the same. The approximate surface velocities obtained from Flierl's model are averaged to be 245 cm/sec. This figure also coincides with Iselin and Fuglister's (1948) measured data. From the same images, the results are different from different models application. Therefore, the choice of the models is very important. The best way to test a model that can be correctly applied to this study area is to have an ocean observation simultaneously by ship and satellite. More reasons concerning the errors made by this method will be discussed in the discussion section.

3.4 Cross-current off Brazos Santiago Entrance Channel

The Brazos Santiago Entrance Channel is the entrance of Port Isabel on the southeastern coast of Texas (Fig. 3.10). It is one of the inlets carrying water in and out of the Laguna Madre. This channel has an average width of 91.5 m (300 ft.) and average depth of 11 m (36 ft) as reported by the Corps of Engineers on April 1, 1971 (see Table 3.4). After examining hundreds of satellite images, mostly from Landsat MSS, I found that the plume jet from this inlet is especially pronounced. It is possibly due to the high content of suspended sediments in the highly polluted water flowing out of the Laguna Madre and the Laguna Madre Channel.

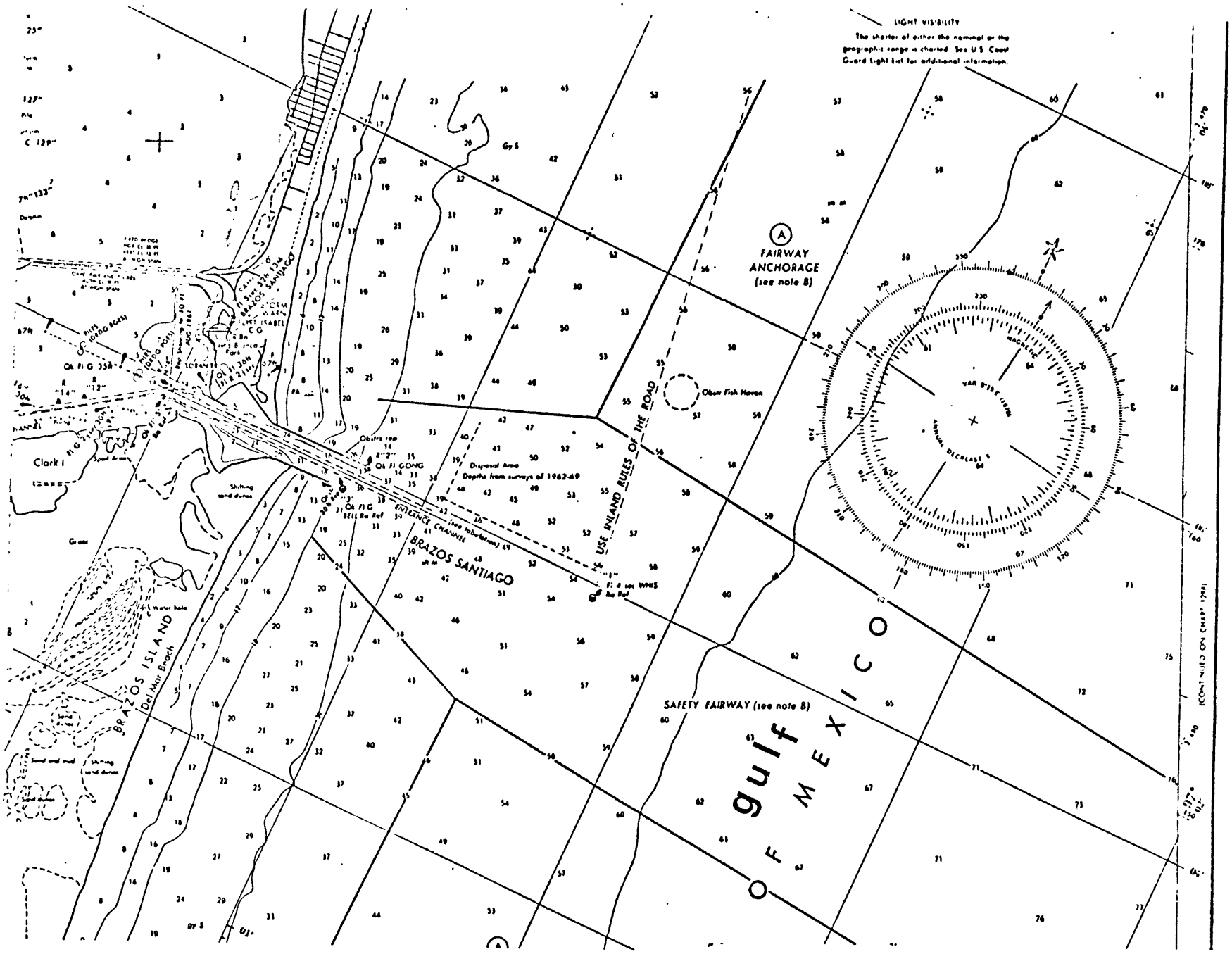

Fig. 3.10 A map showing the location and bathymeters of Brazos Santiago, Texas (after NOAA Nautical Chart No. 898-SC).

The annual average rate of sedimentation exceeds 9 mm/yr close to the inlet and decreases gradually to 4 mm/yr at about 40 km away. This has been determined by 210 Pb isotope dating of cores extending over the past 100 years (see Fig. 3.11). The distribution of the sedimentation rate gives us an indication that the coastal cross-current mostly flows from north to south. The direction and the velocity of the coastal water circulation, as determined by air-drifters at the station have been measured for several years. The seasonal averages for all years are shown in Fig. 3.12. From this figure, we find the trend of the coastal circulation. In the Spring and Summer seasons, the surface currents flow towards the north and in the Fall and Winter seasons toward the south. The strongest current occurs in Spring with an approximate velocity of 10-15 km/day; the weakest current occurs in Winter with an approximate velocity range of 3-8 km/day. Another characteristic of the current drift is that the bottom current directions are 40° to 90° left of the surface direction, except for a few special cases. The average surface velocities in Summer and Fall are approximately 8-12 km/day.

Two of the images that I chose for the purpose of cross-current estimation were taken on Oct. 19, 1978 from Landsat MSS 4 & 5, and are shown in Figs. 3.13 and 3.14. The maximum plume width is estimated by visual interpretation (the image has not digitized in MCIDAS yet) to be 1.5 km. The plume is still visible from the image up to 10 km away from the discharged point. The initial discharged angle with x axis (as defined in Section 2.3) is 90° and the reflected angle at the maximum width is approximately 60° measuring from the enlarged image

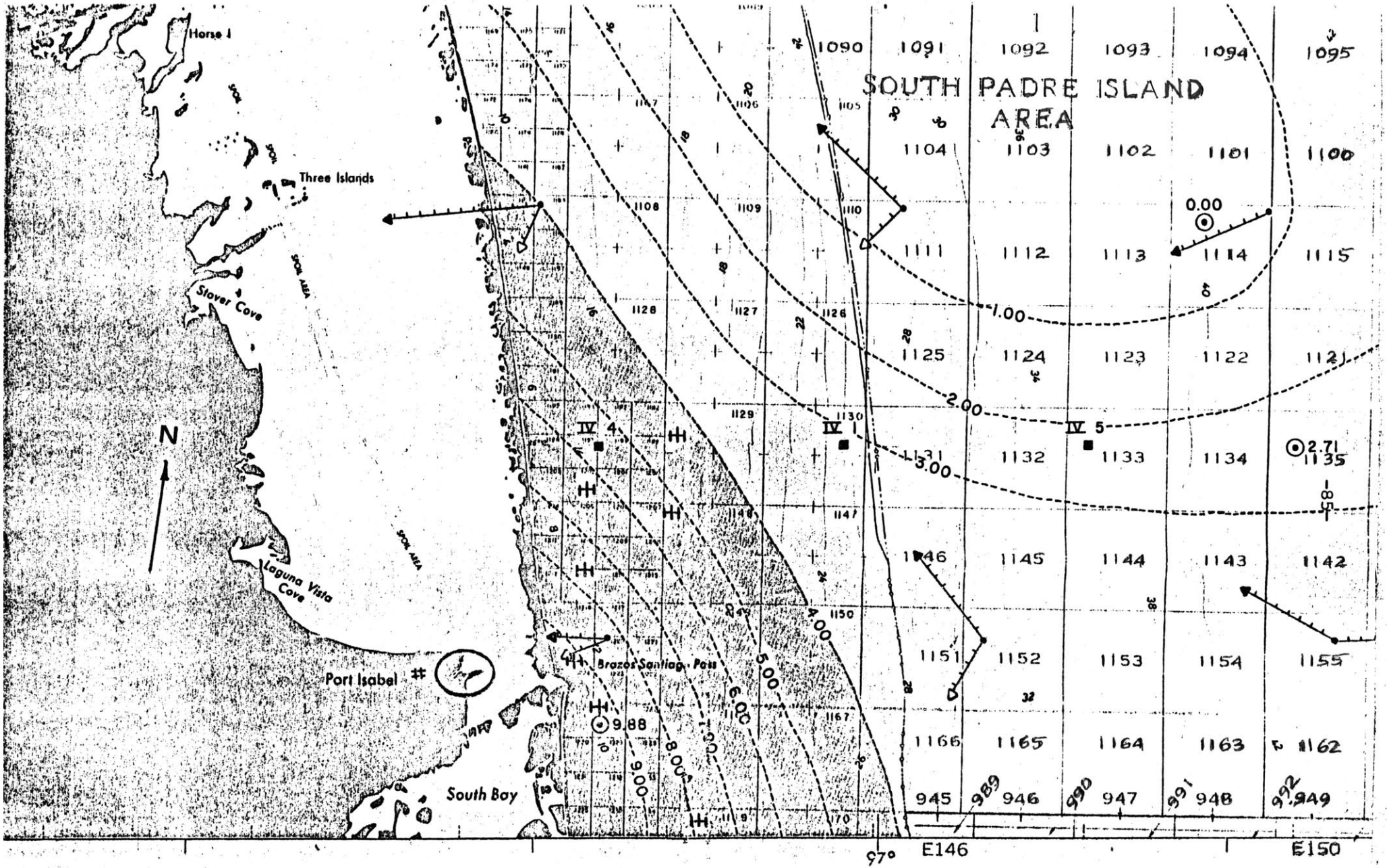

Fig. 3.11 Rate of sedimentation in Brazos Santiago, in mm/yr (after Berryhill & Trippet, 1980).

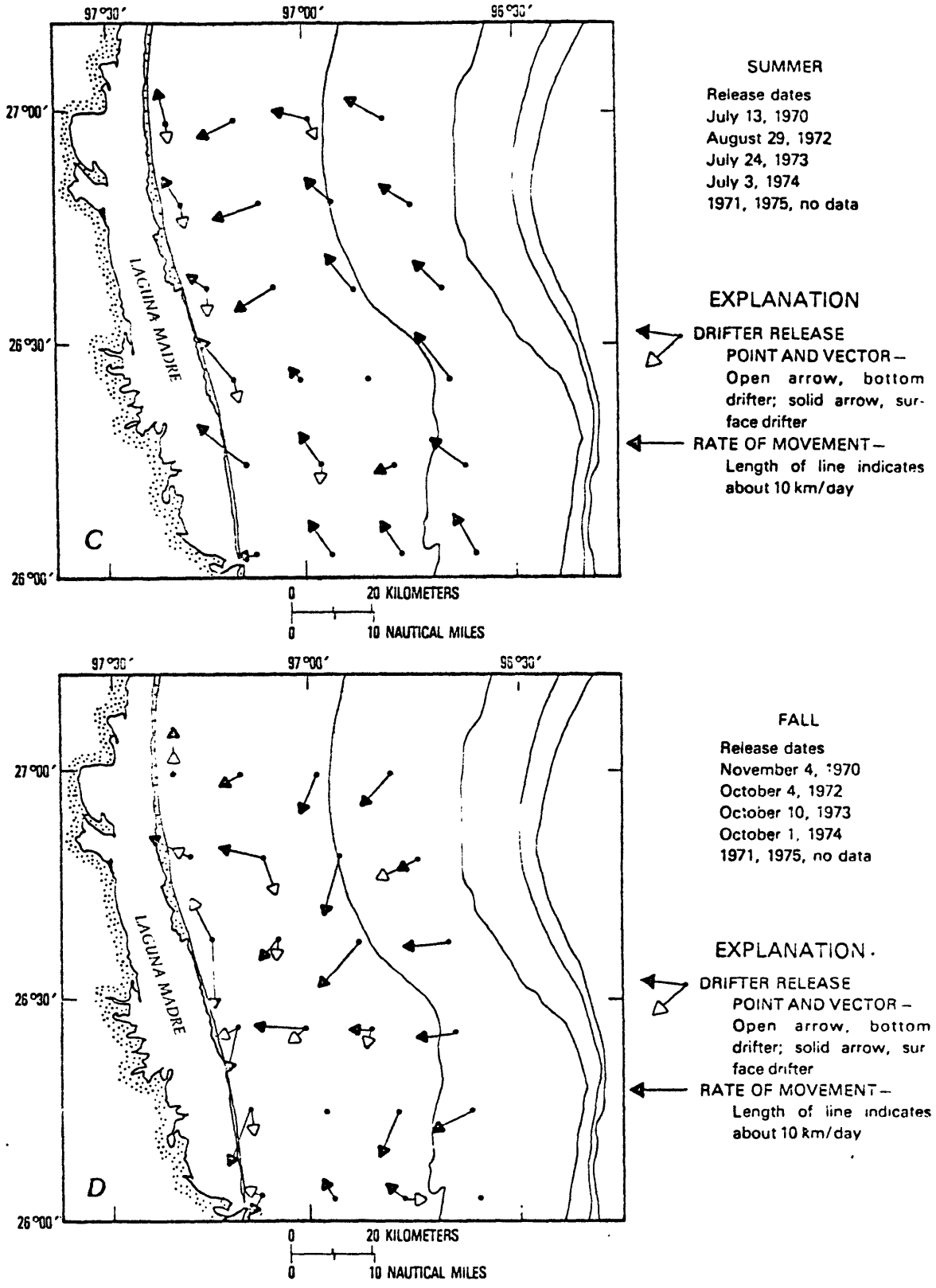

Fig. 3.12a Coastal water circulation of Brazos Santiago, Texas - Summer and Fall - (after Berryhill & Trippet, 1980).

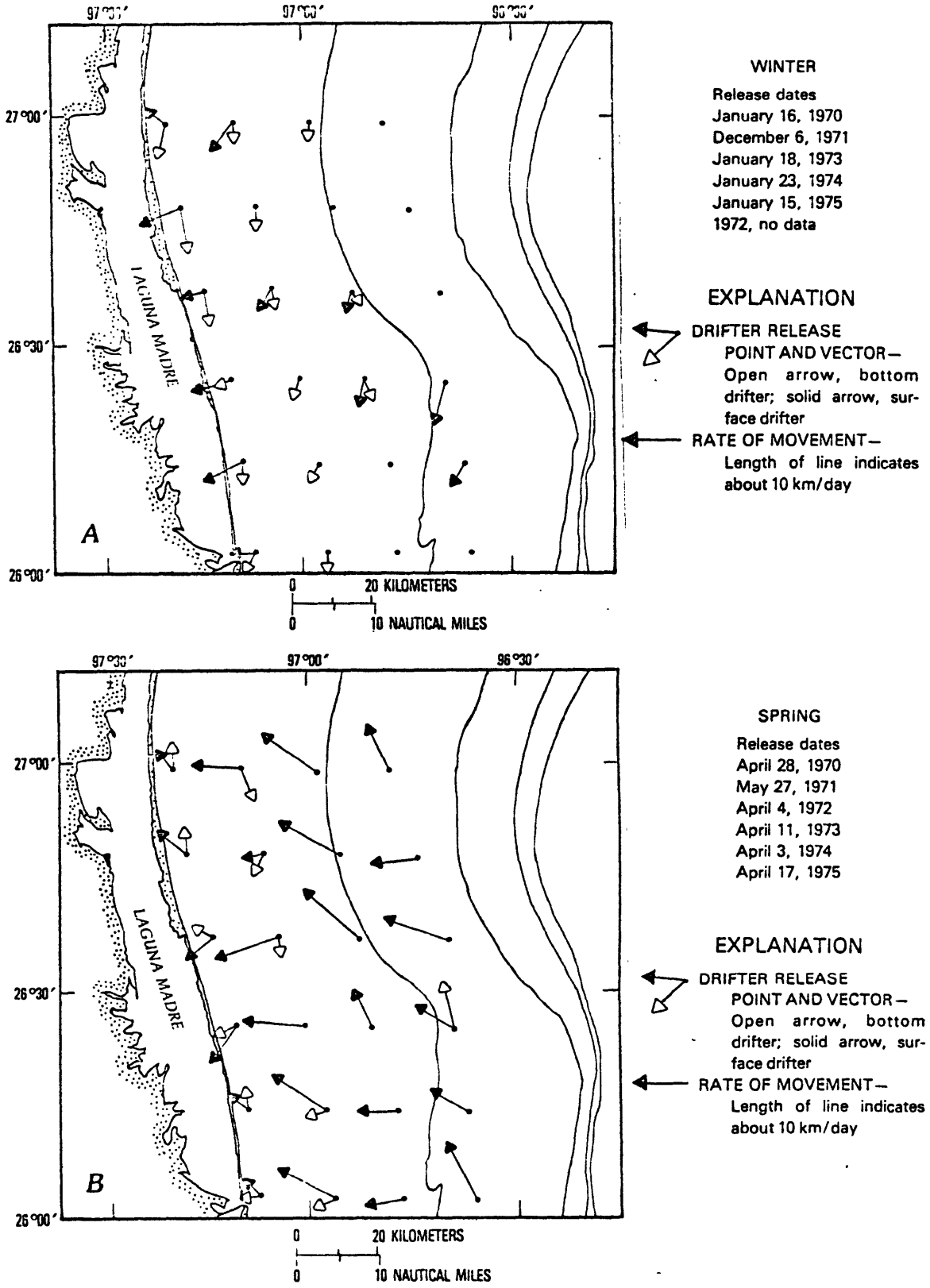

Fig. 3.]2b Coastal water water circulation of Brazos Santiago, Texas - Winter and Spring - (after Berrhill & Trippet,]980).

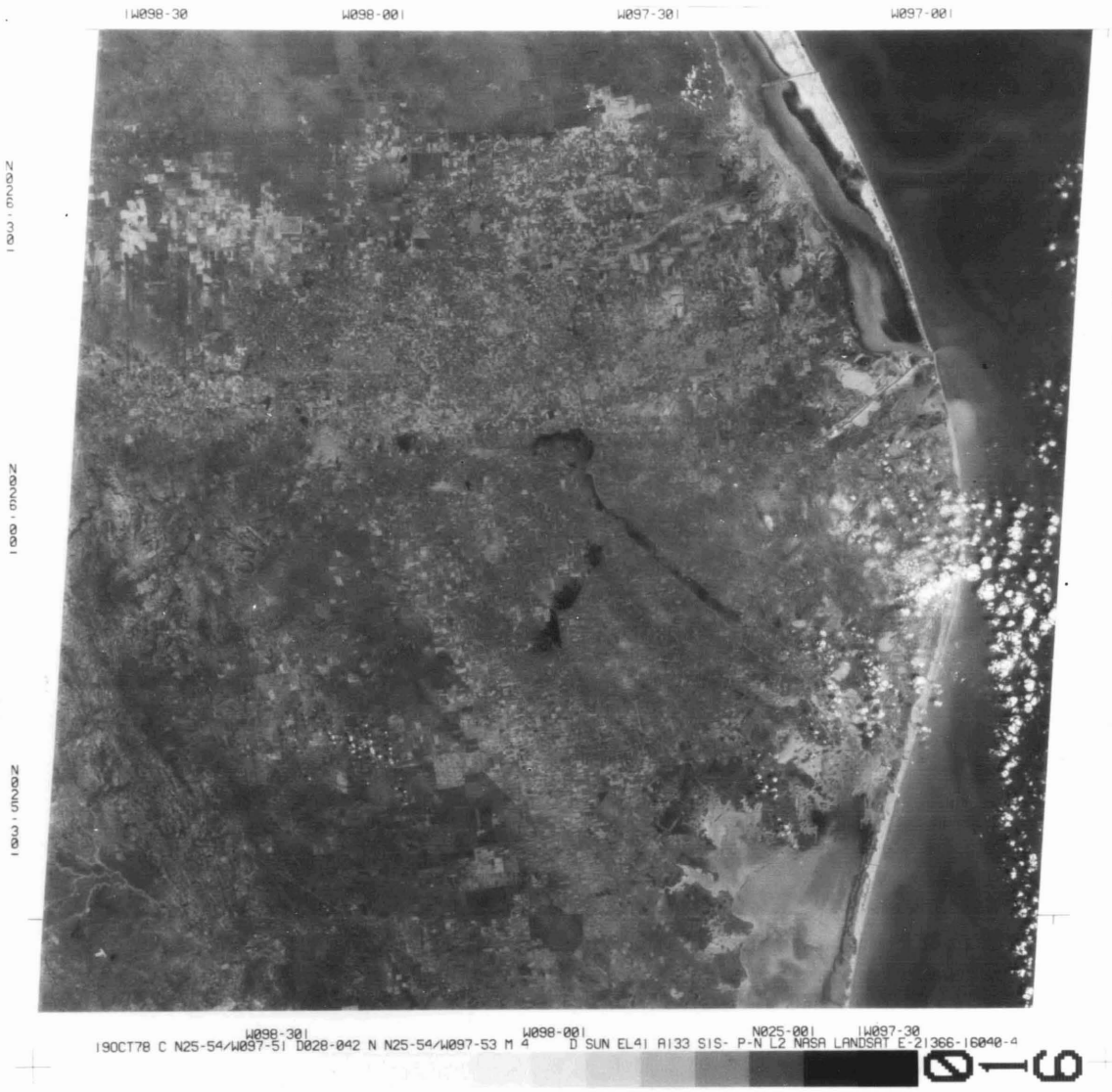

Fig. 3.]3 Landsat MSS-4 image showing plume jets in the eastern coast of Texas, on Oct.]9,]978.

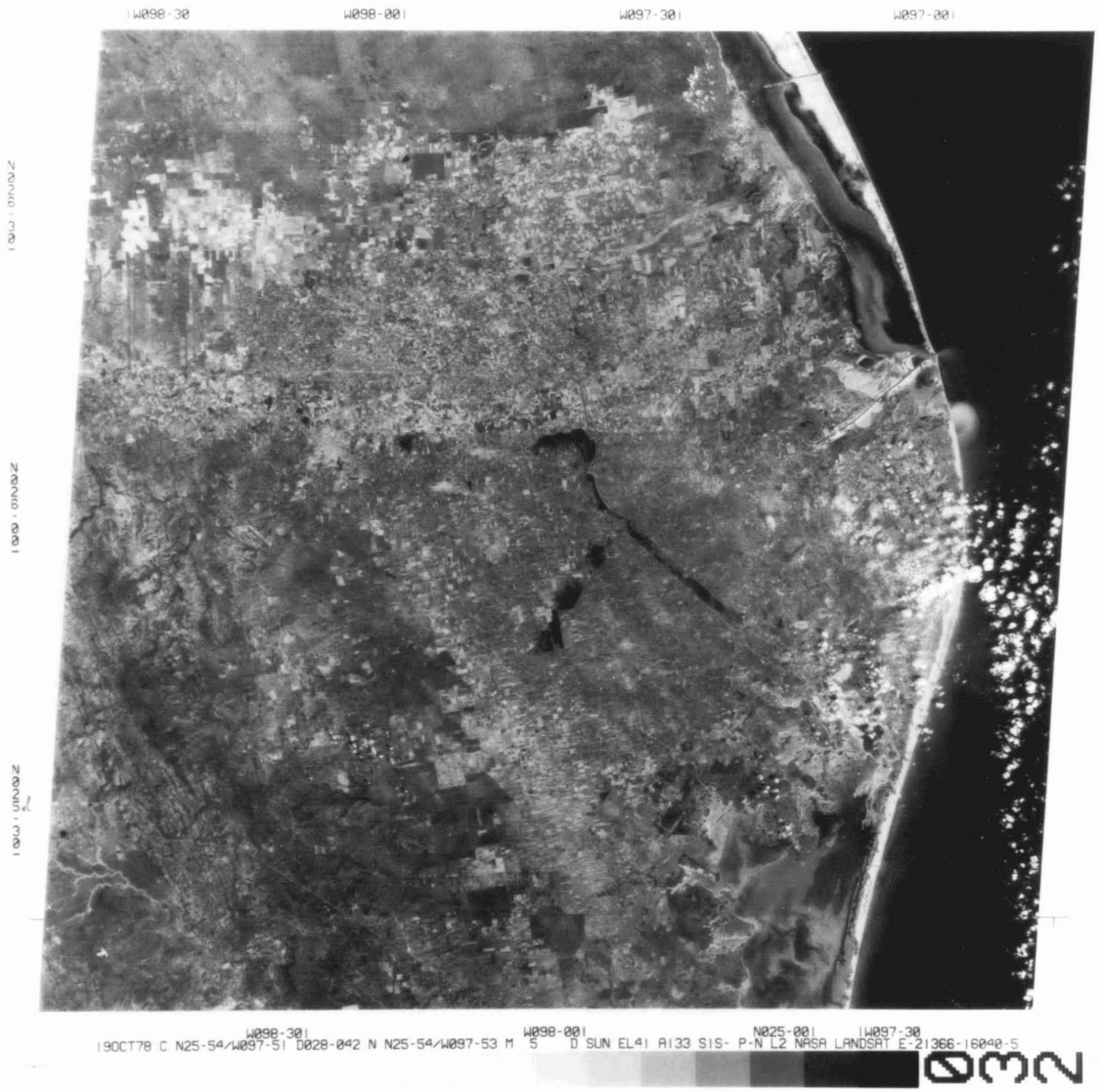

Fig. 3.14 Landsat MSS-5 image showing plume jets in the eastern coast of Texas, on Oct 19, 1978.

Fig. 3.]5 Enlarged image of Landsat MSS-4 in the part of Brazos Santiago, Texas on Oct. 19,]978.

Table 3.4 Some information of Brazos Santiago Entrance Channel (after supplemental data in the NOAA Nautical Chart 898-SC).

BROWNSVILLE AND PORT ISABEL HARBORS CHANNEL DEPTHS

Tabulated from surveys by the Corps of Engineers - report of April 1, 1971

Name of Channel	Controlling depths in channels entering from seaward in feet at Mean Low Water				Existing dredged width (feet)	Project Dimensions	
	Left outside quarter	Middle half of channel	Right outside quarter	Date of Survey		Length (naut. miles)	Depth M.L.W. (feet)
Entrance Channel	36.0	37.5	35.0	3-71	300	1.9	38
Laguna Madre Channel	33.0	36.0	36.0	2-71	200	2.2	36
Brownsville Ship Channel:							
Junction Basin to Boca Chica Passing Basin	37.5	38.0	37.5	2-71	200	3.4	36
Boca Chica Passing Basin to Goose I. Passing Basin	34.0	36.0	33.0	2-71	200	4.5	36
Goose I Passing Basin to Brownsville Turning Basin	36.0	37.0	35.0	2-71	200	2.8	36
Brownsville Turning Basin	35.0	36.0	35.0	2-71	500-1000	1.65	36
Port Isabel Channel	31.0	31.0	29.0	10-70	200	1.0	36
Port Isabel Turning Basin	31.0	31.0	27.0	10-70	1000	0.2	36
Cut Off Channel	31.5	31.0	31.0	10-70	200	0.9	36

Note -The Corps of Engineers should be consulted for changing conditions subsequent to the above.

in Fig. 3.15. Summarizing the above-mentioned

b_o = 45.7 m = 45.7×10^{-3} km

b = 750 m = 0.75 km

h_o = 11 m = 11×10^{-3} km

θ_o = 90°

θ = 60°

x = 5.67 km

I_1 = 0.450 , I_2 = 0.316

From formulas in Section 2.3:

$$b_o/\varepsilon I_2 = 45.7 \times 10^{-3}/0.22 \times .316 = 65.74 \times 10^{-2} \text{ km} < x$$

$$h_o/\varepsilon I_2 = 11 \times 10^{-3}/0.22 \times .316 = 15.82 \times 10^{-2} \text{ km} < x$$

which imply $r = 0$, $s = 0$.

The relation between

$$u_c = u_o \frac{\sqrt{h_o b_o}}{I_2 \varepsilon x} = u_o \frac{\sqrt{11 \times 10^{-3} \times 45.7 \times 10^{-3}}}{0.316 \times 0.22 \times 5.67} = 56.88 \times 10^{-3} u_o$$

$$-\alpha_y = \alpha_z = I_1 \varepsilon/2 = 0.450 \times 0.22/2 = 49.5 \times 10^{-3} \simeq \alpha_{sz}$$

if $\Delta T \simeq 0$

$$\frac{d\theta}{d\tilde{x}} = \frac{d\theta}{dx} \sin\theta = \frac{60-90}{5.67} \sin\theta = -92.18 \times 10^{-3} \sin\theta \text{ rad/km}$$

Substitute in Equation (2.46) with s = r = 0

$$13.93\, u_c^2 - 1828.99\, V u_c + 34.88\, V^2 = 0$$

or

$$45.07 \times 10^{-3}\, u_o^2 - 104.03\, u_o V + 34.88\, V^2 = 0$$

$$V \simeq 2.98\, u_o \qquad \text{for small} \qquad u_o$$

Because observations of the discharged velocity are not available, we can only give an estimate, and assume it to be of the order of 10 km/day. Then $V \simeq 15$ km/day for $u_o = 5$ km/day ; $V \simeq 30$ km/day for $u_o = 10$ km/day. The speed of the coastal current is estimated as ranging from 10 km/day (Fall season) (Berryhill and Trippet, 1980) to 28 km/day (Vukovich, et. al., 1979), which is calculated from the movement of the loop current boundary seen from NOAA and Nimbus infrared data. The estimated data seem to be of the same order of magnitude as the measured ones. However, I have to point out that the formula in Eq. (2.46) is very sensitive to the deflection angle. A small measured error can result in a big error in the estimation of cross-current velocity. Further discussion will be given in the discussion section later.

4. CONCLUSIONS AND DISCUSSION

In an attempt to relate the surface features obtained from a satellite image to ocean surface current velocities, we present three possible simple approaches to enable us to estimate these velocities in the ocean regions at current meandering, eddies, or core rings and a deflected plume jet.

At the current meandering region, a stable and a two-layer baroclinic instability model can be applied for this estimation. When the current meander is wide, the stable approach may be used; otherwise a two-layer baroclinic instability model may be applied. In the application of these two types of instability to the Gulf Stream system off Cape Hatteras, we found that the estimated velocities of the current are around 60 cm/sec for the stable case, and 160 cm/sec for the baroclinic case. The result also shows that the most unstable wavelengths in mode one stay approximately 100 km under the assumption of various mean flow velocities in either layers of the current. The general wavelengths measured from the satellite images off Cape Hatteras are also around 100 km. This fits the two-layer baroclinic instability approach quite well.

A geostrophic approximation eddy model is applied to estimate the maximum tangential velocity and the velocity distributions of an eddy or ring. The estimated maximum tangential velocity in two warm Gulf Stream rings is approximately 180 cm/sec. This result is in good agreement with the local representative data, although this approximation is not thought to be a very representative one in that region.

The cross-current velocity off Brazos Santiago Entrance Channel is also estimated using Stolzenbach and Harloman's model. The estimated cross-current velocities range from 15 to 30 km/day, depending on the discharged velocities of the channel mouth.

To obtain good results from this method, we shall have simple but representative oceanic dynamic approximations and accurate measurements of the oceanic characteristics from a satellite image. These simple approaches should have the relations between current velocity and other oceanic parameters that can be measured from an image. The others are also well-known in that study region. The complicated models are usually not suitable for it, because of too many unknowns in the approach. The ground truth data are essential for this selection. The input parameters of the simple model shall not be very sensitive to the estimation of velocities in case of a small error included in the measurements. The cross-current velocity obtained from a plume jet model is such an example. Because of the difficulty in deflection angle measurement from an image and also many other parameters in higher power, the estimated cross-current velocity is very sensitive to small measurement errors for each parameter. Although it is a good and complete model for a plume jet, it is not necessarily a good model for current estimation. However, except for the doubt about requirements for data quality, this method offers a promising idea for making estimates of ocean surface current from satellite images. Further exploration and improvement of the method are needed because it is also an interesting, convenient and economical way to estimate a surface current without in situ observations.

References

Andrews, J. C. and P. Scully-Power, 1976: The structure of an east Australian Current anticyclonic eddy. J. Phys. Oceanogr., 6 756-765.

Bernstein, R. L., L. Breaker and R. Whritner, 1976: Eddy development in the California Current: ship and satellite results. Science, 195, 353-359.

Bernstein, R. L. and W. B. White, 1974: Time and length scales of baroclinic eddies in the central north Pacific Ocean. J. Phys. Oceanogr., 4, 613-624.

Bernstein, R. L., and W. B. White, 1977: Zonal variability in the distribution of eddy energy in the mid-latitude north Pacific Ocean. J. Phys. Oceanogr., 7, 123-126.

Berryhill, H. L. and A. R. Trippet, 1980: Map showing water circulation and rates of sedimentation in the Port Isabel 1° x 2° Quadrangle, Texas. Miscellaneous Investigations Series, U.S. Geological Survey, 1980.

Boland, F. M. and B. V. Hamon, 1970: The East Australian Current, 1965-1968. Deep-sea Res., 17, 777-794.

Bretherton, F. P. and M. Karweit, 1975: Mid-ocean mesoscale modeling. Proc. Symp. Numerical Models of Ocean Circulation, U.S. Nat. Aca. Sci., Washington, DC.

Carter, H. H., 1969: A preliminary report on the characteristics of a heated jet discharged horizontally into a traverse current. Part I - constant depth. Technical Report 61, Chesepeake Bay Institute, Johns Hopkins University.

Chang, P., S. Pond, and S. Tabata, 1976: Subsurface currents in the Strait of Georgia, West of Sturgeon Bank. J. Fish, Res. Board, Canada, 33, 2218-2241.

Csanady, G. T., 1978: Turbulent interface layer. J. Geophys. Res., 83, 2329-2343.

Csanady, G. T., 1979: The birth and death of a warm core ring. J. Geophys. Res., 84, 777-780.

DeRycke, R. J. and P. K. Rao, 1973: Eddies along a Gulf Stream boundary view from a very high resolution radiometer. J. Phys. Oceanogr., 3, 490-492.

Düing, W. and K-H. Szekielda, 1971: Monsoonal Response in the western Indian Ocean. J. Geophys. Res., 76, 4181-4187.

Dunn, W. E., A. Policastro, and R. A. Paddock, 1975: Surface thermal plumes: Evaluation of mathematical models for the near and complete field. Argonne National Lab., Ill., 420 pp.

Edinger, J. C. and E. M. Polk, Jr., 1969: Initial mixing of thermal discharges into a uniform current. Report No. 1, Department of Environmental and Water Resources Engineering, Vanderbilt University.

Emery, W. J. and L. A. Mysak, 1980: Dynamical interpretation of satellite-sensed thermal features off Vancouver Island. J. Phys. Oceanogr., 10, 961-970.

Flierl, G., 1977: The application of linear quasigeostrophic dynamics to Gulf Stream rings. J. Phys. Oceanogr., 7, 365-379.

Flierl, G., 1979: A simple model for the structure of warm and cold core rings. J. Geophys. Res., 84, 781-785.

Fofonoff, N. P., 1980: The Gulf Stream System, in Evolution of Physical Oceanography, ed. by B. A. Warren and C. Wunsch, M.I.T. Press. 623 pp.

Fuglister, F. C., 1960: Atlantic Ocean Atlas of Termperature and Salinity Profiles and Data from the International Geophysical Year of 1957-1958. Woods Hole Oceanographic Institution, Woods Hole, MA.

Fuglister, F. C., 1963: Gulf Stream'60. Progress in Oceanography, 1, 265-373.

Fuglister, F. C. and A. D. Voorhis, 1965: A new method of tracking the Gulf Stream. Limnol. Oceanogr., 10, Suppl., R. 115-124.

Fuglister, F. C., 1972: Cyclonic rings formed by the Gulf Stream 1965-66. In Studies in Physical Oceanography: A Tribute to Georg Wüst on his 80th Birthday, A. L. Gordon, ed., Gordon and Breach, New York, 1, 137-168.

Fuglister, F. C. and L. V. Worthington, 1951: Some results of a multiple ship survey of the Gulf Stream. Tellus, 3, 1-14.

Gotthardt, G. A., 1973: Observed formation of a Gulf Stream anticyclone eddy. J. Phys. Oceanogr., 3, 237-238, 1973.

Hansen, D. V. and G. A. Maul, 1970: Note on the use of sea surface temperature for observing ocean currents. Remote Sensing of Environment 1, 161-164.

Hoopes, J. A., et. al., 1968: Heat dissipation and induced circulations from condenser cooling water discharges into Lake Monona. Report No. 35, Engineering Experiment Station, University of Wisconsin.

Hunkins, K. L., 1974: Subsurface eddies in the Arctic Ocean. Deep-Sea Res., 21, 1017-1033.

Iselin, C. O'D., 1936: A study of the circulation of the western North Atlantic. Pap. Phys. Oceanogr. and Meteor., 4(4), 101 p.

Iselin, C. O'D. and F. C. Fuglister, 1948: Some recent developments in the study of the Gulf Stream. J. Mar. Res., 7, 317-329.

Kawai, H. 1972: Hydrography of the Kuroshio Extension. In Kuroshio: Physical Aspect of the Japan Current, Ed., H. Stommel and K. Yoshida. University of Washington Press, Seattle and London, 517 pp.

Kitano, K., 1975: Some properties of the warm eddies generated in the confluence zone of the Kuroshio and Oyashio Currents. J. Phys. Oceanogr., 5, 245-252, 1975.

Knauss, J. A., 1969: A note on the transport of the Gulf Stream. Deep-Sea Res., 16 Suppl., 117-123.

LaFond, E. C., 1968: Detailed temperature and current data sections in and near the Kuroshio Current. An Oceanogr. Data Report for CSK, Marine Environment Division, Naval Undersea Center, San Diego. 22 p.

Lee, S. S. and S. Sengupta, 1978: Three dimensional thermal pollution models. NASA CR-154624.

Leitão, C. D. and N. E. Huang, 1979: A note on the comparison of radar altimetry with IR and in situ data for the detection of the Gulf Stream surface boundaries. J. Geophys. Res., 84, 3969-3973.

Malkus, W. V. R., 1953: A recording bathypitotmeter. J. Mar. Res., 12, 51-59.

Masuzawa, J., 1955a: Preliminary report on the Kuroshio in the eastern sea of Japan (Currents and water masses of the Kuroshio System III). Rec. Oceanogr. Wrs. Japan, N.S., 2, 132-140.

Masuzawa, J., 1955b: An outline of the Kuroshio in the eastern sea of Japan (Currents and water masses of the Kuroshi System IV). Oceanogr. Mag., 7, 29-48.

Masuzawa, J., 1956 : A note on the Kuroshio farther to the east of Japan (Currents and water masses of the Kuroshio system VI). Oceanogr. Mag., 7, 97-104.

Maul, G. A. and D. V. Hansen, 1972: An observation of the Gulf Stream surface front structure by ship, aircraft, and satellite. Remote Sensing of Environment, 2, 109-116.

McCreary, J.P. and W. B. White, 1979: On a theory of the Kuroshio meander. Deep-Sea Res., 26A, 317-320.

McGoogan, J. T., 1975: Satellite altimetry applications. IEEE Trans. Microwave Theory Tech., 23, 970-978.

Molinari, R. L., 1970: Cyclonic ring spin-down in the North Atlantic. Ph.D. dissertation. Texas A & M University.

Mollo-Christensen, E., P. Cornillon and A. S. Mascarenhas, Jr., 1981: Method for estimation of ocean current velocity from satellite images. Science, 213, 661-662.

Morgan, G. W., 1956: On the wind-driven ocean circulation. Tellus, 3, 301-320.

Munk, W. H., 1950: On the wind-driven ocean circulation. J. of Meteorology, 7, 79-93.

Mysak, L. A., 1977: On the stability of the California Undercurrent off Vancouver Island. J. Phys. Oceanogr., 7, 904-917.

Mysak, L. A. and F. Schott, 1977: Evidence for baroclinic instability of Norwegian current. J. Geophys. Res., 82,2087-2095.

Nan'niti, T., H. Akamatsu and T. Nakai, 1964: A further observation of a deep current in the East-North-East Sea of Torishima. Oceanogr. Mag., 16, 11-19.

Neuman, G., 1968: Ocean Currents. Elsevier Publishing Company. Amsterdam, London, New York. 352 pp.

Newton, J. L., K. Aagaard and L. K. Coachman, 1974: Baroclinic eddies in the Arctic Ocean. Deep-sea Res., 21, 707-719.

Niiler, P.P., and L. A. Mysak, 1971: Barotropic waves along an eastern continental shelf. Geophys. Fluid Dyn., 2, 273-288.

Nof, D., 1981: On the dynamics of equatorial outflows with application to the Amazon's basin. J. Marine Res., 39, 1-29.

Orlanski, I., 1969: The influence of bottom topography on the stability of jets in a baroclinic fluid. J. Atmos. Sci., 26, 1216-1232.

Orlanski, I., and M. D. Cox, 1973: Baroclinic instability in ocean currents. Geophys. Fluid Dynamics, 4, 297-332.

Otterman, I., 1974: Oceanic eddy in the Gulf of Suez. Deep-Sea Res., 21, 163-165.

Parker, C. E., 1971: Gulf Stream rings in the Sargasso Sea. Deep-Sea Res., 18, 981-993.

Pedlosky, J., 1976: Finite-amplitude baroclinic disturbances in downstream varying currents. J. Phys. Oceanogr., 6, 335-344.

Pedlosky, J., 1979: Geophysical Fluid Dynamics. Springer-Verlag, New York, Heidelberg, Berlin, 624 pp.

Phillips, N., 1966: Large-scale eddy motion in the western Atlantic. J. Geophys. Res., 71, 3883-3891.

Pickard, G. L., 1975: Descriptive physical oceanography. 2nd Edition. Pergamon Press.

Pochasky, T. E., 1966: Measurements of deep water movements with instrumented neutrally buoyant floats. J. Geophys. Res., 71, 2491-2505.

Prych, E., 1973: An analysis of a jet into a turbulent ambient fluid, Water Research 7, Pergamon Press, 647-657.

Rao, P. K., A. E. Strong and R. Koffler, 1971: Gulf Stream meanders and eddies as seen in satellite infrared imagery. J. Phys. Oceanogr., 1, 237-239.

Reid, J., R. A. Schwartzlose and D. Brown, 1963: Direct measurements of a small surface eddy off northern Baja California. J. Marine Res., 21, 205-218.

Richardson, P.L., A. E. Strong, and J. A. Knauss, 1973: Gulf Stream eddies: Recent observations in the western Sargasso Sea. J. Phys. Oceanogr., 3, 297-301.

Saunders, P. M., 1971: Anticyclonic eddies formed from shoreward meander of the Gulf Stream. Deep-Sea Res., 18, 1207-1219.

Schmitz, J. E. and A. C. Vastano, 1975: Entrainment and diffusion in a Gulf Stream cyclonic ring. J. Phys. Oceanogr., 5, 93-97.

Seiwell, H. R., 1939: The effect of short period variation of temperature and salinity of calculations in dynamic oceanography. Pap. Phys. Oceanogr., 7(3), 32 pp.

Sengupta, S. and W. Lick, 1974: A numerical model for wind-driven circulation and temperature fields in lakes and ponds. FTAS/TR-74-99, Case Western Researe University.

Shirazi, M. and L. Davis, 1974: Workbook of thermal plume prediction Volume 2: Surface discharge. Thermal Pollution Branch, Pacific Northwest Environmental Research Laboratory, USEPA, Corvallis, Oregon.

Shoji, D., 1972: Time variation of the Kuroshio south of Japan in Kuroshio, ed., H. Stommel and K. Yoshida. University of Tokyo Press. 517 pp.

Simons, W. F., 1969: A variational method for weak resonant wave interactions. Proc. R. Soc. Lond., A, 309, 551-575.

Solomon, H., 1978: Comments on a thoery of the Kuroshio meander. Deep-Sea Res., 25, 957-958.

Stolzenbach, K. D., and D. R. F. Harleman, 1971: An analytical and experimental discharge of heated water. M.I.T. Department of Civil Engineering, Report No. 135.

Stommel, H., 1948: The westward intensification of wind-driven ocean currents. Transactions, American Geophysical Union, 29, 202-206.

Stommel, H., 1965: The Gulf Stream. University of California Press. Berkeley, 1958, 248 pp.

Stommel, H., P. Niiler, and D. Anati, 1978: Dynamic topography and recirculation of the North Atlantic. J. Marine Res., 36, 449-468.

Strack, S. L., 1953: Surface temperature gradients as indicators of the positions of the Gulf Stream. WHOI Ref. 53-53.

Strazisar, A., and J. Prahl, 1973: The effects of bottom friction on river entrance flow with crossflow. Proc. 16th Conf. Great Lakes Res., 615-625.

Stumpf, H. G., and P. K. Rao, 1975: Evolution of Gulf Stream eddies as seen in satellite infrared imagery. J. Phys. Oceanogr., 5, 388-393.

Swallow, J. C., 1971: The Aries current measurements in the Western North Atlantic. Phil. Trans. Roy. Soc. London, 270, 451-460.

Szekielda, K-H, 1972: Upwelling studies with satellites. J. Cons. Perm. Int. Explor. Mer., 34, 379-388.

Szekielda, K-H., 1976: Space oceanography. Oceanogr. Mar. Biol. Ann. Rev., 14, 99-166.

Taft, B. A., 1978: Structure of Kuroshio south of Japan. J. Mar. Res., 36, 77-117.

Tseng, Y.C., H. M. Inostroza V. and R. Kumar, 1977: Study of the Brazil and Falkland Currents using THIR images of Nimbus V and oceanographic data in 1972 to 1973, Proceedings of the 11th International Symposium on Remote Sensing of Environment, Ann Arbor, MI.

Von Arx, W. S., 1962: An Introduction to Physical Oceanography. Addison-Wesley Publishing Company, Inc. Reading, MA, U.S.A., London, England, 422 pp.

Vukovich, F. M., 1976: An investigation of a cold eddy on the eastern side of the Gulf Stream using NOAA-2 and NOAA-3 satellite data and ship data. J. Phys. Oceanogr., 6, 605-612.

Vukovich, F. M., and B. W. Crissman, 1978: Further studies of a cold eddy on the eastern side of the Gulf Stream using satellite data and ship data. J. Phys. Oceanogr., 8, 838-845.

Vukovich, F. M., and B. W. Crissman, 1980: Some aspects of Gulf Stream western boundary eddies from satellite and in situ data. J. Phys. Oceanogr., 10, 1792-1813.

Vukovich, F. M., B. W. Crissman, M. Bushness, and W. J. King, 1979: Some Aspects of the Oceanography of the Gulf of Mexico using satellite and in situ data. J. Geophys. Res., 84, 7749-7768.

Wada, A., 1968: Studies of prediction of recirculation of cooling water in a bay. Proceedings of the 11th Conference on Coastal Engineering, London.

Waldrop, W., and R. C. Farmer, 1974: Three-dimensional computation of buoyant plumes. J. Geophys. Res., 79, 1269-1276.

Warnecke, G., L. Allison and L. L. Foshee, 1968: Observations of sea surface temperature and ocean currents from Nimbus II. Space Research VIII, North-Holland Publ. Co.

Warnecke, G., L. J. Allison, L. M. McMillin and K.-H. Szekielda, 1971: Remote sensing of ocean currents and sea surface temperature changes derived from Nimbus II satellite. J. Phys. Oceanogr., 1, 45-60.

Warnecke, G., L. M. McMillin and L. J. Allison, 1969: Ocean current and sea surface temperature observations from meteorological satellites. NASA Tech. Note. D-5142, 47 pp.

Warren, B. A., and G. H. Volkmann, 1968: Measurement of volume transport of the Gulf Stream south of New England. J. Mar. Res., 26, 110-126.

White, W. B., and J. P. McCreary, 1976: On the formation of the Kuroshio meander and its relationship to the large-scale ocean circulation. Deep-Sea Res., 23, 33-47.

Wilkerson, J. C., 1967: The Gulf Stream from space. Oceanus, Vol. XIII, Nos. 2 & 3.

Worthington, L. V., 1954: Three detailed cross-sections of the Gulf Stream. Tellus, 6, 116-123.

Worthington, L. V., 1976: On the North Atlantic circulation. The Johns Hopkins University Press, Baltimore and London.

Wyrtki, K., 1962: Geopotential topographies and associated circulation in the western south Pacific Ocean. Aust. J. Marine Freshwater Res., 13, 89-105.